RSC Advances

PAPER

View Article Online
View Journal | View Issue

Check for updates

Cite this: *RSC Adv.*, 2023, **13**, 23514

Achieving above 24% efficiency with non-toxic $CsSnI_3$ perovskite solar cells by harnessing the potential of the absorber and charge transport layers†

M. Khalid Hossain, *[a] M. Shihab Uddin, [b] G. F. Ishraque Toki, [c] Mustafa K. A. Mohammed, [d] Rahul Pandey, [e] Jaya Madan,*[e] Md. Ferdous Rahman, [f] Md. Rasidul Islam, [g] Sagar Bhattarai, [h] H. Bencherif,*[i] D. P. Samajdar, [j] Mongi Amami[k] and D. K. Dwivedi[l]

Lead toxicity is a barrier to the widespread commercial manufacture of lead halide perovskites and their use in solar photovoltaic (PV) devices. Eco-friendly lead-free perovskite solar cells (PSCs) have been developed using certain unique non- or low-toxic perovskite materials. In this context, Sn-based perovskites have been identified as promising substitutes for Pb-based perovskites due to their similar characteristics. However, Sn-based perovskites suffer from chemical instability, which affects their performance in PSCs. This study employs theoretical simulations to identify ways to improve the efficiency of Sn-based PSCs. The simulations were conducted using the SCAPS-1D software, and a lead-free, non-toxic, and inorganic perovskite absorber layer (PAL), *i.e.* $CsSnI_3$ was used in the PSC design. The properties of the hole transport layer (HTL) and electron transport layer (ETL) were tuned to optimize the performance of the device. Apart from this, seven different combinations of HTLs were studied, and the best-performing combination was found to be ITO/PCBM/$CsSnI_3$/CFTS/Se, which achieved a power conversion efficiency (PCE) of 24.73%, an open-circuit voltage (V_{OC}) of 0.872 V, a short-circuit current density (J_{SC}) of 33.99 mA cm^{-2} and a fill factor (FF) of 83.46%. The second highest PCE of 18.41% was achieved by the ITO/PCBM/$CsSnI_3$/CuSCN/Se structure. In addition to optimizing the structure of the PSC, this study also analyzes the current density–voltage (J–V) along with quantum efficiency (QE), as well as the impact of series resistance, shunt resistance, and working temperature, on PV performance. The results demonstrate the potential of the optimized structure identified in this study to enhance the standard PCE of PSCs. Overall, this study provides important insights into the development of lead-free absorber materials and highlights the potential of using $CsSnI_3$ as the PAL in PSCs. The optimized structure identified in this study can be used as a base for further research to improve the efficiency of Sn-based PSCs.

Received 2nd May 2023
Accepted 19th July 2023

DOI: 10.1039/d3ra02910g

rsc.li/rsc-advances

Open Access Article. Published on 04 August 2023. Downloaded on 2/24/2026 8:13:02 PM.
This article is licensed under a Creative Commons Attribution-NonCommercial 3.0 Unported Licence.

[a]*Institute of Electronics, Atomic Energy Research Establishment, Bangladesh Atomic Energy Commission, Dhaka 1349, Bangladesh. E-mail: khalid.baec@gmail.com; khalid@kyudai.jp*

[b]*Department of Electrical and Electronic Engineering, Islamic University, Kushtia 7000, Bangladesh*

[c]*College of Materials Science and Engineering, Donghua University, Shanghai 201620, China*

[d]*University of Warith Al-Anbiyaa, 56001 Karbala, Iraq*

[e]*VLSI Centre of Excellence, Chitkara University Institute of Engineering and Technology, Chitkara University, Punjab 140401, India. E-mail: jaya.madan@chitkara.edu.in*

[f]*Advanced Energy Materials and Solar Cell Research Laboratory, Department of Electrical and Electronic Engineering, Begum Rokeya University, Rangpur 5400, Bangladesh*

[g]*Department of Electrical and Electronic Engineering, Bangamata Sheikh Fojilatunnesa Mujib Science & Technology University, Jamalpur 2012, Bangladesh*

[h]*Technology Innovation and Development Foundation, Indian Institute of Technology Guwahati, Guwahati 781039, Assam, India*

[i]*LEREESI, Higher National School of Renewable Energies, Environment and Sustainable Development, Batna 05078, Algeria. E-mail: bencherif.hichem@hns-re2sd.dz*

[j]*Dept. of ECE, Indian Institute of Information Technology, Design & Manufacturing, Madhya Pradesh 482005, India*

[k]*Department of Chemistry, College of Sciences, King Khalid University, P.O. Box 9004, Abha, Saudi Arabia*

[l]*Department of Physics and Material Science, Madan Mohan Malaviya University of Technology, Gorakhpur, 273010, U.P., India*

† Electronic supplementary information (ESI) available. See DOI: https://doi.org/10.1039/d3ra02910g

© 2023 The Author(s). Published by the Royal Society of Chemistry

Open Access Article. Published on 04 August 2023. Downloaded on 2/24/2026 8:13:02 PM. This article is licensed under a Creative Commons Attribution-NonCommercial 3.0 Unported Licence.

1 Introduction

To meet the huge energy crisis of the 21st century, the popularity of perovskite[1,2] and thin-film solar cells has been channelized toward the efficient production of renewable solar energy, which has shown an exponential growth rate in the last few years. Among the various types of solar cells, perovskite solar cells (PSCs) have become predominant for their ideal tunable bandgaps, long diffusion length, better carrier transfer and ease of fabrication.[3–9] It has also been noticed in recent studies that $MAPbI_3$ is conventionally used in perovskite solar cells since its introduction in 2009 by Kojima *et al.*[10] Extensive research also confirms that lead (Pb)-based PSCs have higher efficiencies than those based on Pb-free perovskites.[11,12] Despite the advantage of efficiency, the toxicity of Pb and environmental issues are always a concern while using these perovskites. To overcome these problems, researchers have proposed Pb-free perovskites, which provide greater efficiency.[13,14] A few metals, such as Sn, Ge, Bi, Sb, and Cu, can be utilized instead of Pb for the synthesis of metal hybrid perovskites. Over the past few years, tin (Sn)-based perovskites are used greatly amongst these metals because of their improved optical[15] and electronic properties, such as higher charge mobility and narrow bandgaps.[16–18] Meanwhile, the chemical instability of the crystal structure and the mismatch of energy levels between the absorber layer and charge transport layer are the main drawbacks of Sn-based perovskites that impede them from achieving higher efficiencies. Therefore, lead-free, non-volatile $CsSnI_3$ can be used as the perovskite absorber material (PAL).

However, at the moment, simple oxidation of Sn^{2+} is the fundamental issue that prevents the development of $CsSnI_3$-based PSCs. The devices nonetheless operate poorly despite carrying out the whole manufacturing process in an inert environment because a trace amount of oxidation products already exists in the solution used as the precursor. B–$CsSnI_3$ easily degrades in the ambient environment to form the yellow polymorph $CsSnI_3$ and then Cs_2SnI_6, which contains tetravalent tin. Compared with B–$CsSnI_3$, Cs_2SnI_6 has a significantly reduced light-harvesting capability.[19] Consequently, the poor device stability, as well as low power conversion efficiency, of $CsSnI_3$-based solar cells is caused by the unintended oxidation of Sn^{2+} to Sn^{4+}, which significantly reduces their application potential in the photovoltaic field. The precursor state is where Sn^{2+} oxidation is about to take place, mostly in three ways. The first possibility is Sn^{2+} self-disproportionation, which results in Sn^{4+} and Sn_0.[20] The second is oxidation by dimethylsulfoxide (DMSO), a popular solvent for Sn-based perovskites.[21] The third method is oxidation by the extremely little quantity of oxygen added to the precursor solution. According to a new report by Marshall *et al.*, adding $SnCl_2$ as an additive to perovskite photovoltaics (PPV) based on $CsSnI_3$ results in higher efficiency, as well as improved device stability.[22] Their findings might represent progress towards lead-free perovskite PPVs. For a $CsSnI_3$ thin-film photovoltaic, Hatton and colleagues evaluated the effect of a number of tin halide additives, including SnF_2, $SnCl_2$, $SnBr_2$, and SnI_2, which showed encouraging results.[22]

$CsSnI_3$ is a prototypical single halide perovskite with the formula of AMX_3, where A denotes a monovalent inorganic/organic cation (such as Cs^+, MA^+, FA^+), M denotes a divalent cation (such as Pb^{2+}, Sn^{2+}, Ge^{2+}) and X denotes a halogen anion (such as I^-, Br^-, Cl^-).[23] Among the monovalent cations, Cs^+ could provide better power conversion efficiency (PCE) because of its higher stability than MA^+ and FA^+ when used as a cation in the PSC.[24–26] Chen *et al.* have reported that despite having a smaller bandgap of 1.3 eV, a PCE of 12.92% was achieved when $CsSnI_3$ was used as the PAL.[16–18] On the contrary, Song *et al.* found that the low efficiency for the absorber $CsSnI_3$ was 3.83% in comparison to other reported studies.[27] The absorber layer is placed in between the hole transport layer (HTL) and the electron transport layer (ETL) and helps in the transfer of holes and electrons in the entire device,[28–32] whereas the ETL helps the extraction and transport of electrons[33] in PSCs and eliminates electrical shunts between the transparent electrode and the perovskite layer. An ideal ETL should have high electron mobility and hole-blocking properties, which can also prevent potential reactions between the cathode and the perovskite layer.[34] Among the many organic and inorganic ETL materials, phenyl-C61-butyric acid methyl ester (PCBM) has been utilized widely over the years due to the reduced number of film defects and, by extension, less unwanted electron–hole recombination between the perovskite layer and the electrode with the ETL. Since it is crucial to achieve a homogeneous and pin-hole-devoid PCBM layer, some attempts to enhance PCBM layers have been made by employing processing methods, such as refining the spin-coating rates and solvents. According to Bai *et al.*, PCBM used as the ETL in the PSC device improved the efficiency up to 9.56%.[35]

On the other hand, the HTL generally aids in extracting and transporting the holes[36] in the absorber layer to the electrode and functions as an energy barrier to prevent electron transport to the anode.[37] In Sn-based PSCs, the energy levels of ITO and the PAL do not match, which results in decreased hole collection and photovoltaic (PV) outputs.[38] Therefore, the HTL should match the energy level of the PAL and possess high hole mobility for transporting holes to the anode along with a low absorption coefficient.[39] Similar to the ETL, some organic and inorganic HTLs, such as Spiro-MeOTAD, PEDOT:PSS, P3HT, NiO, CuI, CuSCN, and CFTS (Cu_2FeSnS_4), are frequently utilized in various solar cells.[40–49] Amongst these HTLs, Spiro-MeOTAD and PEDOT:PSS are being used widely in most PSCs due to their high performance. However, among all these HTLs, CFTS provides the best efficiency probably due to the low energy level difference between $CsSnI_3$ and CFTS.[39]

In our previous study,[50] we evaluated the suitability of a variety of ETLs and HTLs from 70 different configurations to find the ideal combination for the $CsSnI_3$ absorber layer-based PSC to achieve good PV performance. In this study, $CsSnI_3$ is used as the lead-free PAL to bring out the best configurations from the previous study[50] and optimize various parameters toward increasing the device efficiency, for the very first time, by combining the PCBM ETL with various HTLs, including Spiro-MeOTAD, PEDOT:PSS, P3HT, NiO, CuI, CuSCN, and CFTS, *via* SCAPS-1D (one-dimensional solar cell capacitance simulator)

Open Access Article. Published on 04 August 2023. Downloaded on 2/24/2026 8:13:02 PM.
This article is licensed under a Creative Commons Attribution-NonCommercial 3.0 Unported Licence.

software. Because of the time and effort required to investigate all these materials, getting the best possible result from scientific experiments can be difficult. Only a few theoretical and experimental studies have been done on $CsSnI_3$-based PSCs, offering many opportunities to improve their performance. Here, the maximum efficiency of the non-toxic Sn-based $CsSnI_3$ PSC is targeted by varying different features, including the back metal contact, PAL, ETL, and HTL, using the SCAPS-1D simulation software. Additionally, the influence of series resistance, shunt resistance, and working temperature on the PV performance of the PSC have been investigated besides the current density–voltage and quantum efficiency (QE) parameters. Finally, the resulting highly efficient devices are contrasted against earlier experiments in terms of their capacity to improve the typical PCE.

2 Materials and methodology

2.1 SCAPS-1D numerical simulation

The SCAPS-1D software was introduced by Professor M. Burgelman at the University of Gent and has been used to simulate different solar cell configurations.[51–59] The SCAPS-1D simulator uses fundamental semiconductor equations, in terms of the Poisson equations (eqn 1), and continuity equations for excitons (electrons and holes).[60,61]

$$\frac{d^2}{dx^2}\Psi(x) = \frac{e}{\varepsilon_0\varepsilon_r}\left(p(x) + N_D + \rho_p - n(x) - N_A - \rho_n\right) \quad (1)$$

where Ψ denotes the electrostatic potential, e denotes electron charge, ε_0 denotes vacuum permittivity, ε_r denotes relative permittivity, N_D and N_A denote donor and acceptor densities, respectively, p denotes the hole concentration, n denotes the electron concentration, ρ_p denotes the hole distribution, and ρ_n denotes the electron distribution.

The continuity equation for an electron is represented below (eqn (2)),

$$-\frac{dJ_n}{dx} = G - R \quad (2)$$

where, J_n is the electron current density, G is the generation rate, and R is the recombination rate.

The continuity equation for holes is given by eqn (3),

$$\frac{dJ_p}{dx} = G - R \quad (3)$$

where J_p is the hole current density.

The drift and diffusion equations are given by eqn (4) and (5), respectively,

$$J_n = D_n\frac{dn}{dx} + \mu_n n\frac{d\varphi}{dx} \quad (4)$$

$$J_n = D_p\frac{dp}{dx} + \mu_p p\frac{d\varphi}{dx} \quad (5)$$

where $D_{n(p)}$ is the diffusion coefficient of an electron (hole) and $\mu_{n(p)}$ is the electron (hole) mobility. SCAPS works in one-dimensional and steady-state conditions.

2.2 The $CsSnI_3$-based perovskite solar cell structure

The structure consisted of ITO, which was used as the transparent conductive oxide (TCO), the ETL, PAL, HTL, and lastly a back metal contact. The PAL was sandwiched between the ETL and the HTL. The ETL helps in extracting, collecting and transferring electrons, and HTL works on blocking electrons and collecting holes from the PAL and transferring these holes to the cathode. The structure of our solar cell was ITO/ETL/$CsSnI_3$/HTL/Se. Fig. 1 shows the configuration of the $CsSnI_3$-based solar cell used in this simulation.

Here, initially, the PCBM ETL was combined with different HTLs (CuSCN, NiO, P3HT, PEDOT:PSS, Spiro-MeOTAD, CuI, and CFTS) along with a fixed PAL ($CsSnI_3$) and back metal contact (Au). After that, the back metal contact (like Au, W, Ni, Pd, Pt, Se, Ag, C, Fe, and Cu) was varied to obtain the optimum structure among the seven studied structures. Then, the input parameters, such as the thickness of PAL, ETL, and HTL, the collective impact of PAL and HTL acceptor and defect density, the ETL donor and defect density, and interface defects were further optimized stepwise, and the optimized outcomes were added progressively with the other optimized parameters in this study. The study was carried out at the illumination of AM1.5 and the solar irradiation intensity of 100 mW cm^{-2}. In Tables 1 and 2, the input parameters utilized in the simulation are summarized. While Table 1 represents the values of the different parameters of ITO, the ETL (PCBM), the PAL ($CsSnI_3$), and different HTLs, Table 2 represents the values of the interface defects.

3 Result and discussion

3.1 The influence of $CsSnI_3$ thickness and the acceptor doping density on PV performance

Research on PSCs has seen tremendous progress in recent years, achieving higher efficiency and potential for low-cost

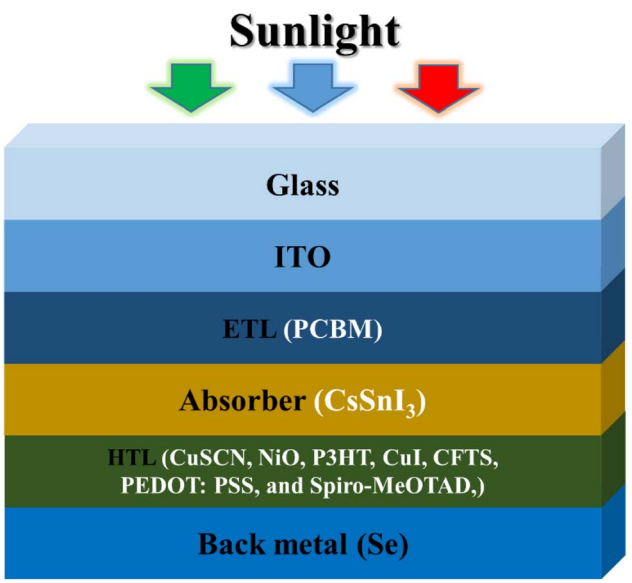

Fig. 1 Configuration of $CsSnI_3$ solar cells used in this numerical simulation.

© 2023 The Author(s). Published by the Royal Society of Chemistry

Open Access Article. Published on 04 August 2023. Downloaded on 2/24/2026 8:13:02 PM. This article is licensed under a Creative Commons Attribution-NonCommercial 3.0 Unported Licence.

Table 1 The input parameters of TCO, ETL (PCBM), HTLs, and PAL ($CsSnI_3$).[50]

Parameters	ITO	CuSCN	PCBM	P3HT	PEDOT:PSS	Spiro-MeOTAD	NiO	CuI	CFTS	$CsSnI_3$
Thickness (nm)	500	50	50	50	50	200	100	100	100	800[a]
E_g (eV)	3.5	3.6	2	1.7	1.6	3	3.8	3.1	1.3	1.3
X (eV)	4	1.7	3.9	3.5	3.4	2.2	1.46	2.1	3.3	3.6
ε_r	9	10	3.9	3	3	3	10.7	6.5	9	9.93
N_C (cm^{-3})	2.2×10^{18}	2.2×10^{19}	2.5×10^{21}	2×10^{21}	2.2×10^{18}	2.2×10^{18}	2.8×10^{19}	2.8×10^{19}	2.2×10^{18}	1×10^{19}
N_v (cm^{-3})	1.8×10^{19}	1.8×10^{18}	2.5×10^{21}	2×10^{21}	1.8×10^{19}	1.8×10^{19}	1×10^{19}	1×10^{19}	1.8×10^{19}	1×10^{18}
μ_n ($cm^2\ V^{-1}\ s^{-1}$)	20	100	0.2	1.8×10^{-3}	4.5×10^{-2}	2.1×10^{-3}	12	100	21.98	1.5×10^{3}
μ_h ($cm^2\ V^{-1}\ s^{-1}$)	10	25	0.2	1.86×10^{-2}	4.5×10^{-2}	2.16×10^{-3}	2.8	43.9	21.98	5.85×10^{2}
N_A (cm^{-3})	0	1×10^{18}	0	1×10^{18}	1×10^{18}	1.0×10^{18}	1×10^{18}	1.0×10^{18}	1×10^{18}	10^{20}
N_D (cm^{-3})	1×10^{21}	0	2.93×10^{17}	0	0	0	0	0	0	0
N_t (cm^{-3})	1×10^{15}[a]	1×10^{15}[a]	1×10^{15}[a]	1×10^{15}[a]	1×10^{15}[a]	1.0×10^{15}[a]	1×10^{15}[a]	1.0×10^{15}[a]	1×10^{15}[a]	1×10^{15}[a]

[a] In this study, these values remained constant during initial optimization to get the best combination of HTL, ETL, and Back metal contact.

Table 2 The input parameters of the interface defect layers.[50]

Interface	Defect type	Capture cross section: electrons/holes (cm^2)	Energetic distribution	Reference for defect energy level	Total density (cm^{-2}) (integrated overall energies)
ETL/$CsSnI_3$	Neutral	1.0×10^{-17} / 1.0×10^{-18}	Single	Above the VB maximum	1.0×10^{10}
$CsSnI_3$/HTL	Neutral	1.0×10^{-18} / 1.0×10^{-19}	Single	Above the VB maximum	1.0×10^{10}

production. However, to further enhance the performance and stability of PSCs, it is essential to examine the impact of various parameters on device performance. Two such parameters are absorber thickness and acceptor doping density, which are critical to optimizing the efficiency of PSCs. The absorber thickness in PSCs plays a substantial role in determining the efficiency of the device. The optimal thickness of the absorber layer is determined by the bandgap and absorption coefficient of the material, which dictate the amount of light that can be absorbed by the device. A thick absorber layer may increase the photon absorption rate, but it can also lead to an increased recombination rate, which would reduce the efficiency of the device. Conversely, a thinner absorber layer may reduce the photon absorption rate but can also reduce the recombination rate and improve device efficiency. Acceptor doping density is another critical parameter that affects the performance of PSCs. Doping acceptor atoms into the absorber layer can modify the band structure and improve the carrier transport properties of the device. However, excessive doping can lead to increased defects and reduced carrier lifetimes, which negatively impact the device efficiency. Therefore, optimization of the acceptor doping density is crucial to achieving high device efficiency.

A combined study of absorber thickness and acceptor doping density is essential for optimizing the performance of PSCs. By optimizing both parameters simultaneously, it is possible to achieve the highest possible device efficiency. The absorber thickness must be optimized to balance the photon absorption and recombination rates, while the acceptor doping density must be carefully controlled to minimize the influence of defects on device performance. Therefore, a collective study of the effects of absorber thickness and acceptor doping density was carried out. Fig. 2–5 illustrate the changes in the PV characteristics, namely V_{OC}, J_{SC}, FF, and PCE, of the solar cell with the variation of the absorber layer acceptor density and thickness; while the absorber layer was varied from 100 nm to 1300 nm, the acceptor density (N_A) was varied from 1×10^9 cm^{-3} to 1.0×10^{21} cm^{-3}.

The dependency of the V_{OC} of the ITO/PCBM/$CsSnI_3$/CFTS/Se device is shown in Fig. 2(a). Here, the highest V_{OC} of 0.927 V was achieved at a thickness <800 nm and $N_A > 8 \times 10^{20}$ cm^{-3} and started declining before and after 800 nm thickness. The lowest value of V_{OC} *i.e.* 0.827 V was recorded at thickness >1000 nm. From Fig. 2(b), while using CuI as the HTL, the highest V_{OC} of >0.914 V was achieved at thickness <200 nm and N_A of $>1.0 \times 10^{21}$ cm^{-3}. With the increase in thickness to >200 nm and decrease in N_A to $<8.0 \times 10^{20}$ cm^{-3}, the value of V_{OC} dropped from 0.889 V to 0.826 V.

Similarly, Fig. 2(c) and (e)–(g) demonstrate that the V_{OC} of these configurations varied from 0.826 V to 0.927 V in the presence of other tested HTLs except NiO. The highest V_{OC} of >0.914 V was achieved at thickness <200 nm and $N_A > 1.0 \times 10^{21}$ cm^{-3}. With the increase in thickness to >200 nm and a decrease in N_A to $<8.0 \times 10^{20}$ cm^{-3}, the values of V_{OC} dropped from 0.889 V to 0.826 V. On the contrary, while using NiO as the HTL, the V_{OC} varied from 0.839 V to 0.927 V, as seen in Fig. 2(d), while the highest V_{OC} of >0.914 V was achieved at absorber thickness <600 nm and $N_A < 8.0 \times 10^{20}$ cm^{-3}. With the increase in thickness to values >800 nm and decrease in N_A below 8.0×10^{20} cm^{-3}, the value of V_{OC} dropped from 0.894 V to 0.839 V (Fig. 2(d)).

The dependency of J_{SC} of the device ITO/PCBM/$CsSnI_3$/CFTS/Se is shown in Fig. 3(a). From the figure, it is evident that J_{SC}

Open Access Article. Published on 04 August 2023. Downloaded on 2/24/2026 8:13:02 PM.
This article is licensed under a Creative Commons Attribution-NonCommercial 3.0 Unported Licence.

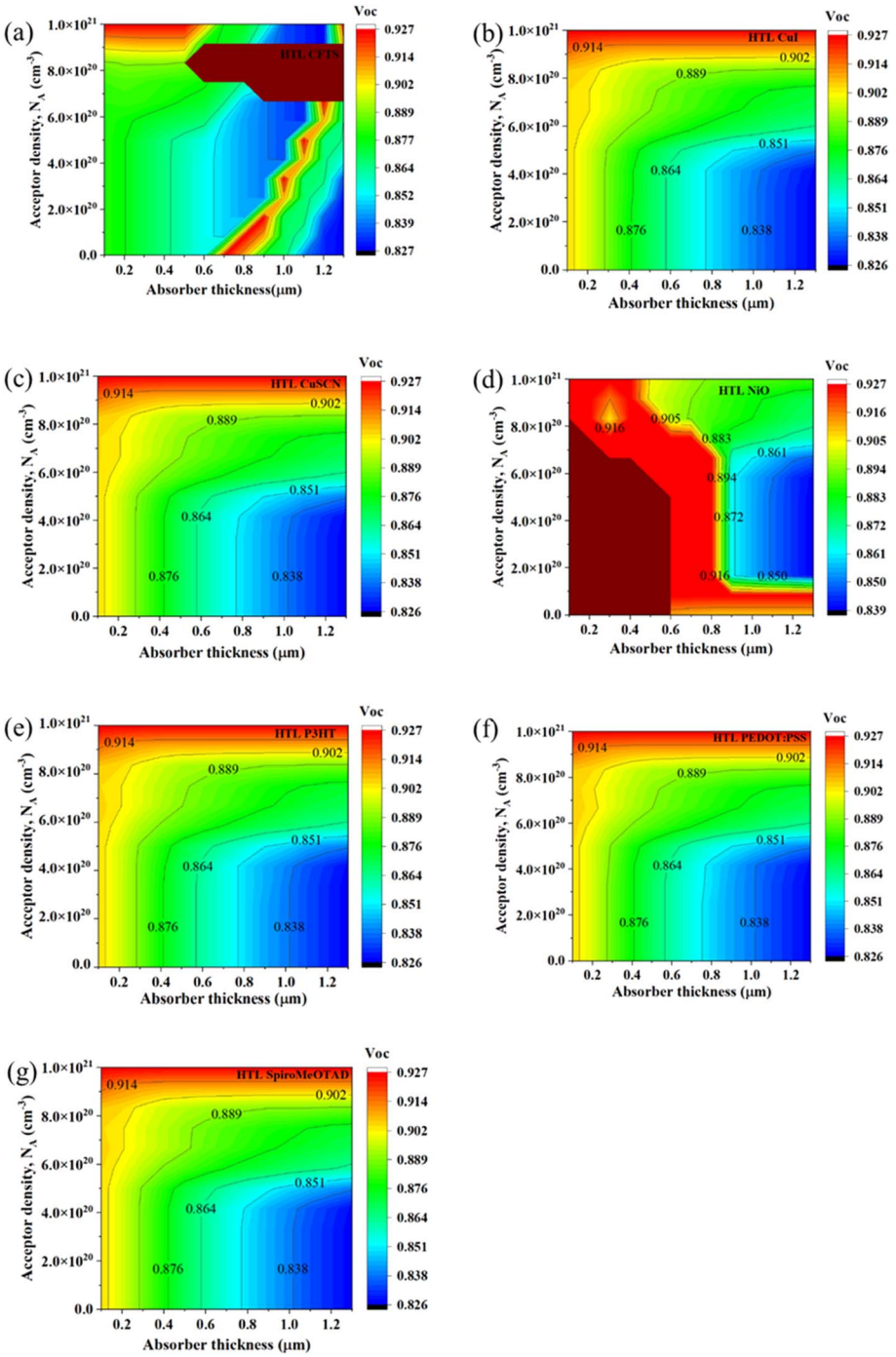

Fig. 2 (a)–(g) Contour graphs of the dependency of the V_{OC} of PSCs with different HTLs on the thickness and acceptor density of the absorber.

varied from 6.20 mA cm^{-2} to 34.10 mA cm^{-2}. The highest J_{SC} values > 30.61 mA cm^{-2} were achieved at thicknesses <800 nm, and they were independent of N_A. At higher N_A < 8.0 × 10^{20} cm^{-3}, the value of J_{SC} dropped from 20.15 mA cm^{-2} to 6.20 mA cm^{-2}. Similarly, Fig. 3(b) demonstrates the J_{SC} variation of the device with CuI as the HTL from 6.20 mA cm^{-2} to 34.30 mA cm^{-2}. At thickness >400 nm and N_A < 8.0 ×10^{20} cm^{-3}, J_{SC} increased from 27.28 mA cm^{-2} to 34.30 mA cm^{-2}. At higher N_A < 8.0 × 10^{20} cm^{-3}, the value of J_{SC} dropped from 20.25 mA cm^{-2} to 6.2 mA cm^{-2}. Similarly, Fig. 3(c), (e) and (f) illustrate that J_{SC} varied from 6.20 mA cm^{-2} to 34.30 mA cm^{-2} in the presence of other HTLs except NiO. At thickness >400 nm and N_A < 8.0 × 10^{20} cm^{-3}, J_{SC} increased from 27.28 mA cm^{-2} to 34.30 mA cm^{-2}. At higher N_A < 8.0 × 10^{20} cm^{-3}, the value of J_{SC} dropped from 20.25 mA cm^{-2} to 6.20 mA cm^{-2}.

On the other hand, from Fig. 3(d), it can be seen that J_{SC} varied from 6.20 mA cm^{-2} to 34 mA cm^{-2} when NiO was employed as the HTL. At thickness >800 nm, J_{SC} gradually

© 2023 The Author(s). Published by the Royal Society of Chemistry

Open Access Article. Published on 04 August 2023. Downloaded on 2/24/2026 8:13:02 PM.
This article is licensed under a Creative Commons Attribution-NonCommercial 3.0 Unported Licence.

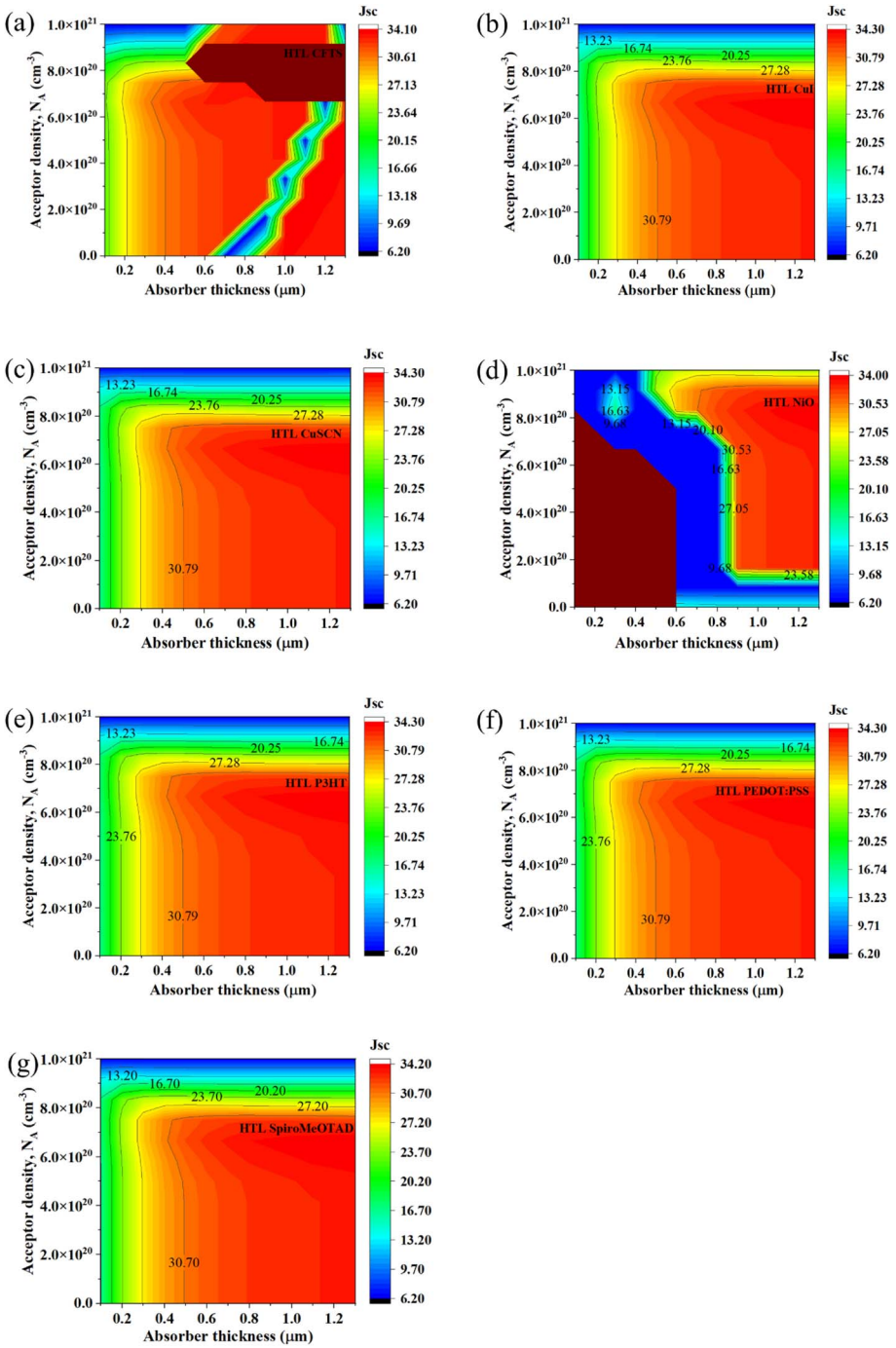

Fig. 3 (a)–(g) Contour graphs of the dependency of the J_{SC} of PSCs with different HTLs on the thickness and acceptor density of the absorber.

decreased from 16.63 mA cm^{-2} to 6.20 mA cm^{-2}. At thicknesses higher than 800 nm, the value of J_{SC} increased from 20.10 mA cm^{-2} to 34.00 mA cm^{-2}. The dependency of J_{SC} of the device ITO/PCBM/$CsSnI_3$/Spiro-MeOTAD/Se is shown in Fig. 3(g); in this case, J_{SC} varied from 6.20 mA cm^{-2} to 34.20 mA cm^{-2}. At thickness >400 nm and $N_A < 8.0 \times 10^{20}$ cm^{-3}, J_{SC} increased from 27.20 mA cm^{-2} to 34.20 mA cm^{-2}. At higher $N_A < 8.0 \times 10^{20}$ cm^{-3}, the value of J_{SC} dropped from 23.70 mA cm^{-2} to 6.20 mA cm^{-2}.

The dependency of the FF for the device with the ITO/PCBM/$CsSnI_3$/CFTS/Se structure is shown in Fig. 4(a), and FF varied from 74.58% to 80.90%. At thickness <400 nm and $N_A < 6.0 \times 10^{20}$ cm^{-3}, the device showed maximum FF values >80.11%, and with the increase in thickness and N_A, it gradually decreased from 78.53% to 74.58%. Fig. 4(b) demonstrates that FF varied from 73.60% to 82.60% while using CuI as the HTL; at thickness >300 nm and $N_A < 6.0 \times 10^{20}$ cm^{-3}, the FF of the device increased from 80.35% to 82.60% but with further

Open Access Article. Published on 04 August 2023. Downloaded on 2/24/2026 8:13:02 PM.
This article is licensed under a Creative Commons Attribution-NonCommercial 3.0 Unported Licence.

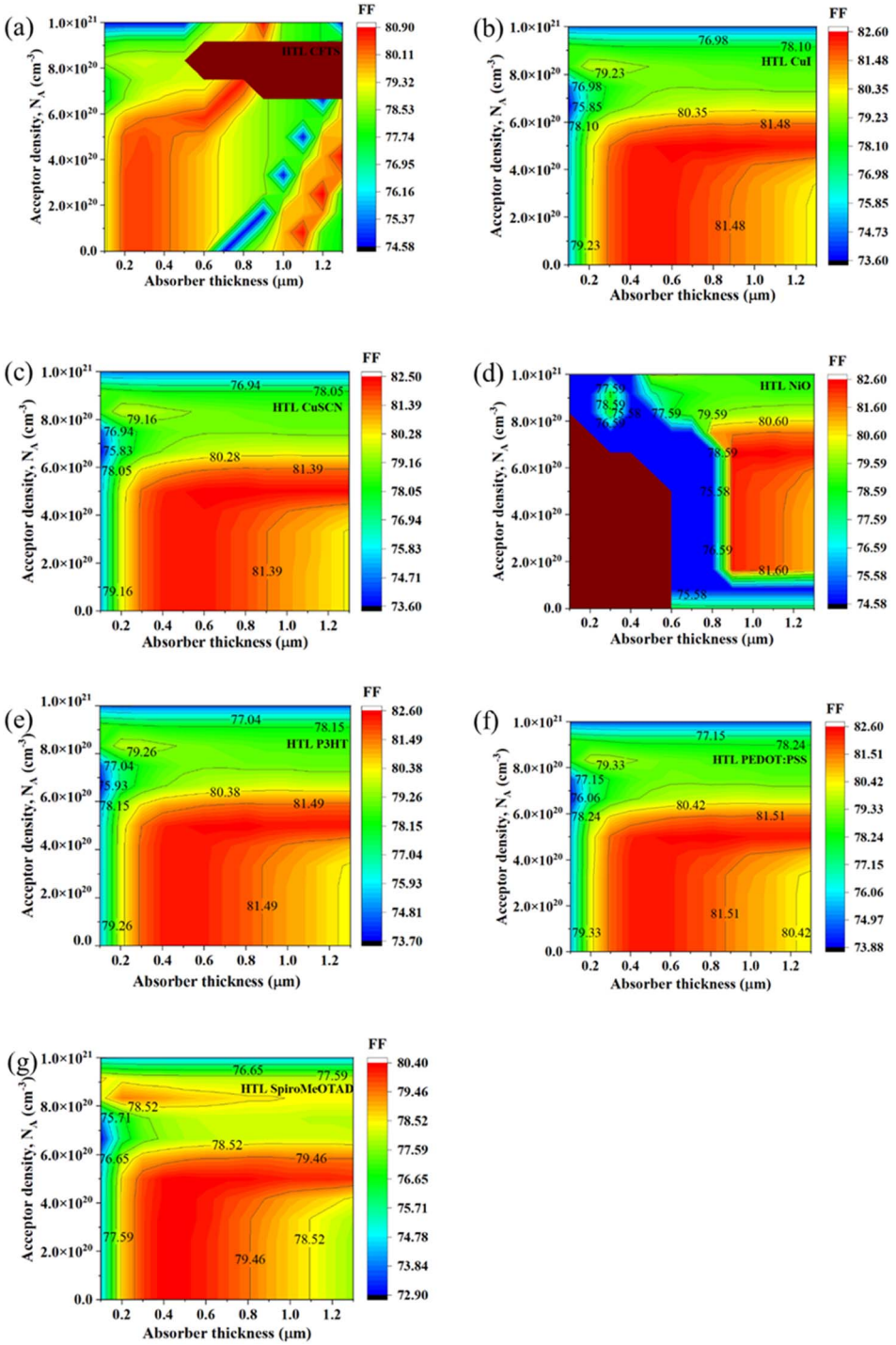

Fig. 4 (a)–(g) Contour graphs of the dependency of the FF of PSC with different HTLs on the acceptor density and thickness of the absorber.

increase in thickness to >1000 nm, the FF tended to decline. At thickness <200 nm and $N_A > 6.0 \times 10^{20}$ cm^{-3}, respectively, the FF decreased from 80.35% to 73.60%. Similarly, from Fig. 4(e) and (f), it can be seen that FF varied from 73.70% to 82.60% for P3HT (Fig. 4(e)) and 73.88% to 82.60% for PEDOT:PSS (Fig. 4(f)). Meanwhile at thickness >300 nm and $N_A < 6.0 \times 10^{20}$ cm^{-3}, the FF of the devices increased from 80.88% to 82.60%, but a further increase in thickness to >1000 nm led to a decline in FF. Moreover, at thickness and <200 nm and $N_A > 6.0 \times 10^{20}$ cm^{-3}, respectively, the FF decreased up to 73.70% and 73.88% (Fig. 4(e) and (f)).

In contrast, Fig. 4(c), illustrates that FF varied from 73.60% to 82.50% when the CuSCN HTL was employed. At thickness >300 nm and $N_A < 6.0 \times 10^{20}$ cm^{-3}, the FF of the device increased from 80.28% to 82.50%. However, a further increase in thickness to >1000 nm caused an FF decline. At thickness

© 2023 The Author(s). Published by the Royal Society of Chemistry

Open Access Article. Published on 04 August 2023. Downloaded on 2/24/2026 8:13:02 PM.
This article is licensed under a Creative Commons Attribution-NonCommercial 3.0 Unported Licence.

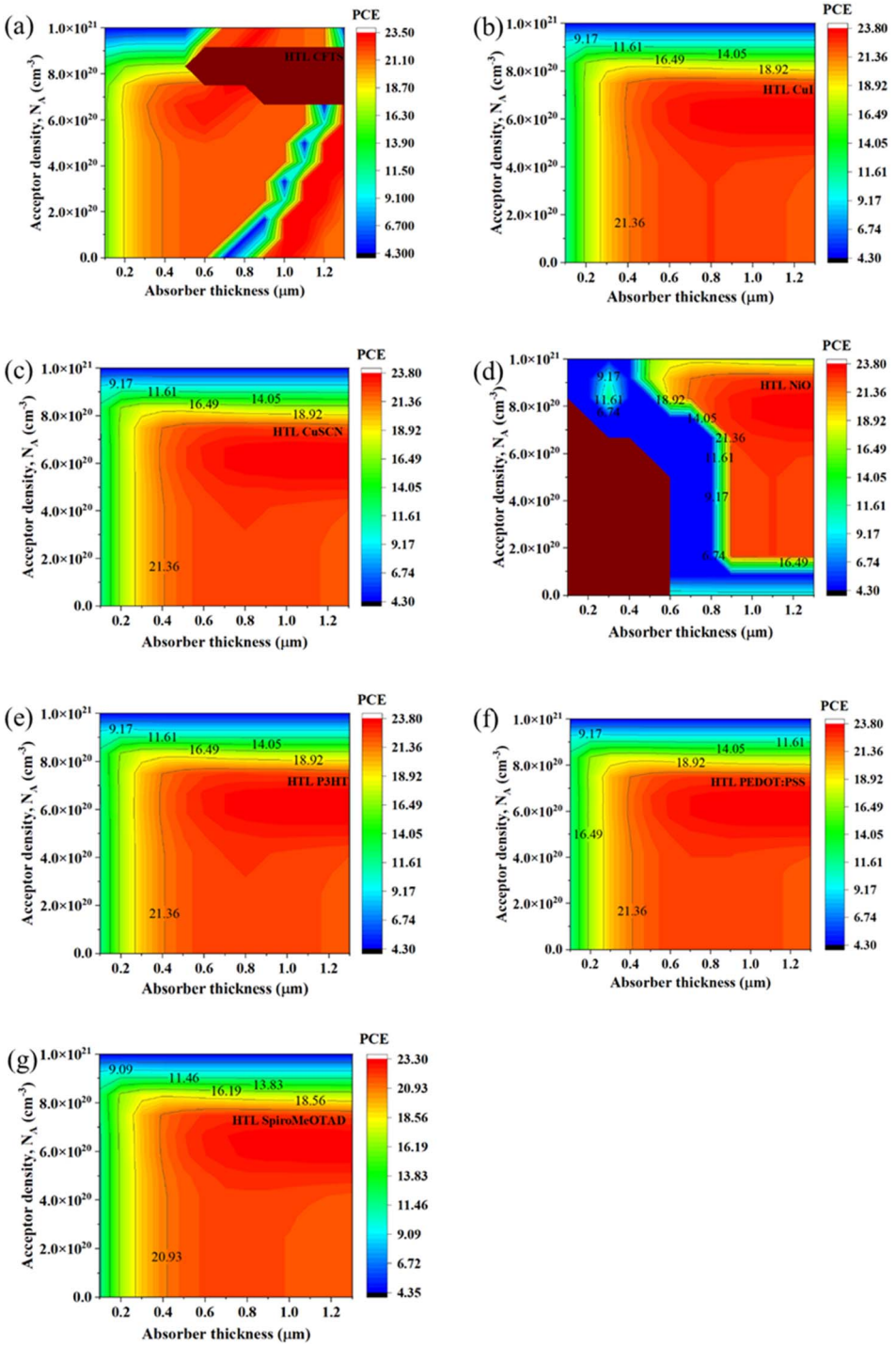

Fig. 5 (a)–(g) Contour graphs of the dependency of the PCE of PSCs with different HTLs on the thickness and acceptor density of the absorber.

<200 nm and N_A > 6.0 × 10^{20} cm^{-3}, respectively, the FF decreased from 80.28% to 73.60%. From Fig. 4(d), it can be seen that the FF varied from 74.58% to 82.60% with the NiO HTL. In particular, at thickness <800 nm, the FF of the device decreased from 79.59% to 74.58%, but a further increase in thickness to >900 nm causes the FF to rise in the range of 2.0 × 10^{20} cm^{-3} to 8.0 × 10^{20} cm^{-3}. Further, the FF values of the ITO/PCBM/$CsSnI_3$/Spiro-MeOTAD/Se device varied from 72.90% to 80.40%; at thickness >200 nm and N_A < 6.0 × 10^{20} cm^{-3}, its FF increased from 78.52% to 80.40%, but a further increase in thickness to >900 nm caused FF to decline. At thickness <200 nm and N_A > 6.0 × 10^{20} cm^{-3} respectively, FF decreased to 72.90% (Fig. 4(g)).

The dependency of the PCE of the ITO/PCBM/$CsSnI_3$/CFTS/Se device is shown in Fig. 5(a). From the figure, it can be seen that its PCE varied from 4.3% to 23.50%. At thickness >200 nm and N_A < 6.0 × 10^{20} cm^{-3}, the PCE of the device increased from

Open Access Article. Published on 04 August 2023. Downloaded on 2/24/2026 8:13:02 PM.
This article is licensed under a Creative Commons Attribution-NonCommercial 3.0 Unported Licence.

18.70% to 23.50%, and with the decrease in thickness and increase in N_A, the PCE gradually decreased from 18.70% to 4.30%. A similar trend of PCE was seen in the other devices except for that using the Spiro-MeOTAD HTL, as shown in Fig. 5(b)–(f). For all these devices, PCE varied from 4.3% to 23.80%. At thickness >200 nm and N_A of < 8.0×10^{20} cm^{-3}, the PCE of the devices increases from 18.92% to 23.80%. At lower thicknesses <200 nm and N_A of < 8.5×10^{20} cm^{-3}, the PCE values decreased from 16.49% to 11.61%, and with a further increase in the value of N_A, the PCE dropped to 4.3% independent of thickness variation. Moreover, the PCE for the device of ITO/PCBM/$CsSnI_3$/Spiro-MeOTAD/Se is shown in Fig. 5(g), which was the lowest among all the structures. It was noticed that its PCE varied from 4.35% to 23.30%. At thickness >200 nm and N_A < 8.0×10^{20} cm^{-3}, the PCE of this device increased from 18.56% to 23.30%. At lower thicknesses <200 nm and N_A of <

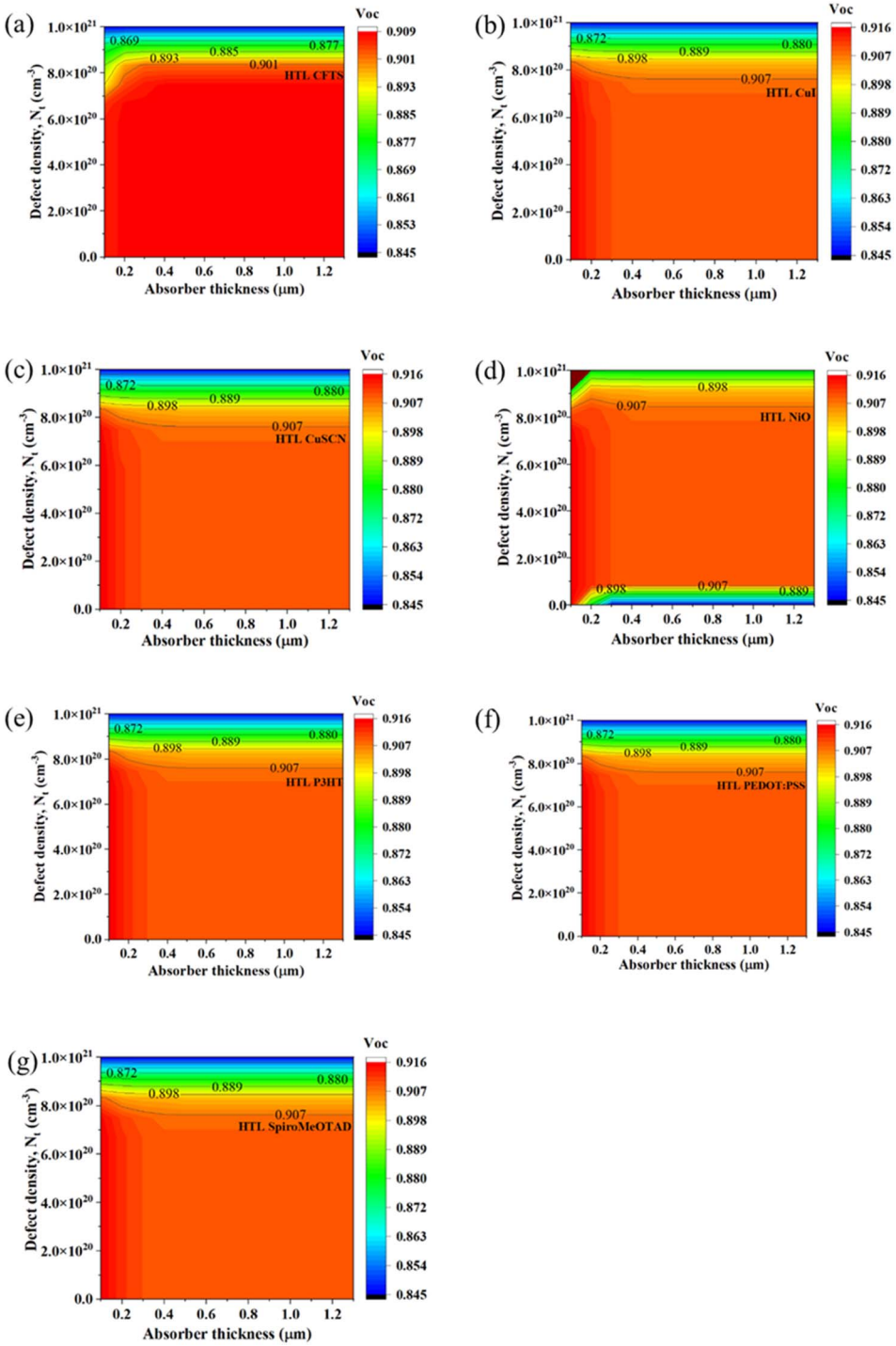

Fig. 6 (a)–(g) Contour graphs of the dependency of the V_{OC} of PSCs with different HTLs on the defect density and thickness of the PAL.

© 2023 The Author(s). Published by the Royal Society of Chemistry

Open Access Article. Published on 04 August 2023. Downloaded on 2/24/2026 8:13:02 PM.
This article is licensed under a Creative Commons Attribution-NonCommercial 3.0 Unported Licence.

8.5×10^{20} cm^{-3}, the PCE decreased from 16.19% to 11.46%, but with a further increase in the value of N_A, the PCE dropped to 4.35% independent of the thickness variation.

3.2 The influence of $CsSnI_3$ thickness and defect density

Defect density is another essential parameter that affects the performance of PSCs. Defects in the absorber layer act as recombination centers, thereby reducing the carrier lifetime and efficiency of the device. Therefore, controlling the defect density of the absorber layer is crucial to achieving high device efficiency. The influence of $CsSnI_3$ absorber thickness and defect density on PSC performance has been extensively studied, and it has been shown that the two parameters are interrelated. By optimizing both parameters simultaneously, it is possible to achieve the highest possible device efficiency. The optimal $CsSnI_3$ thickness and defect density depend on the specific material and device

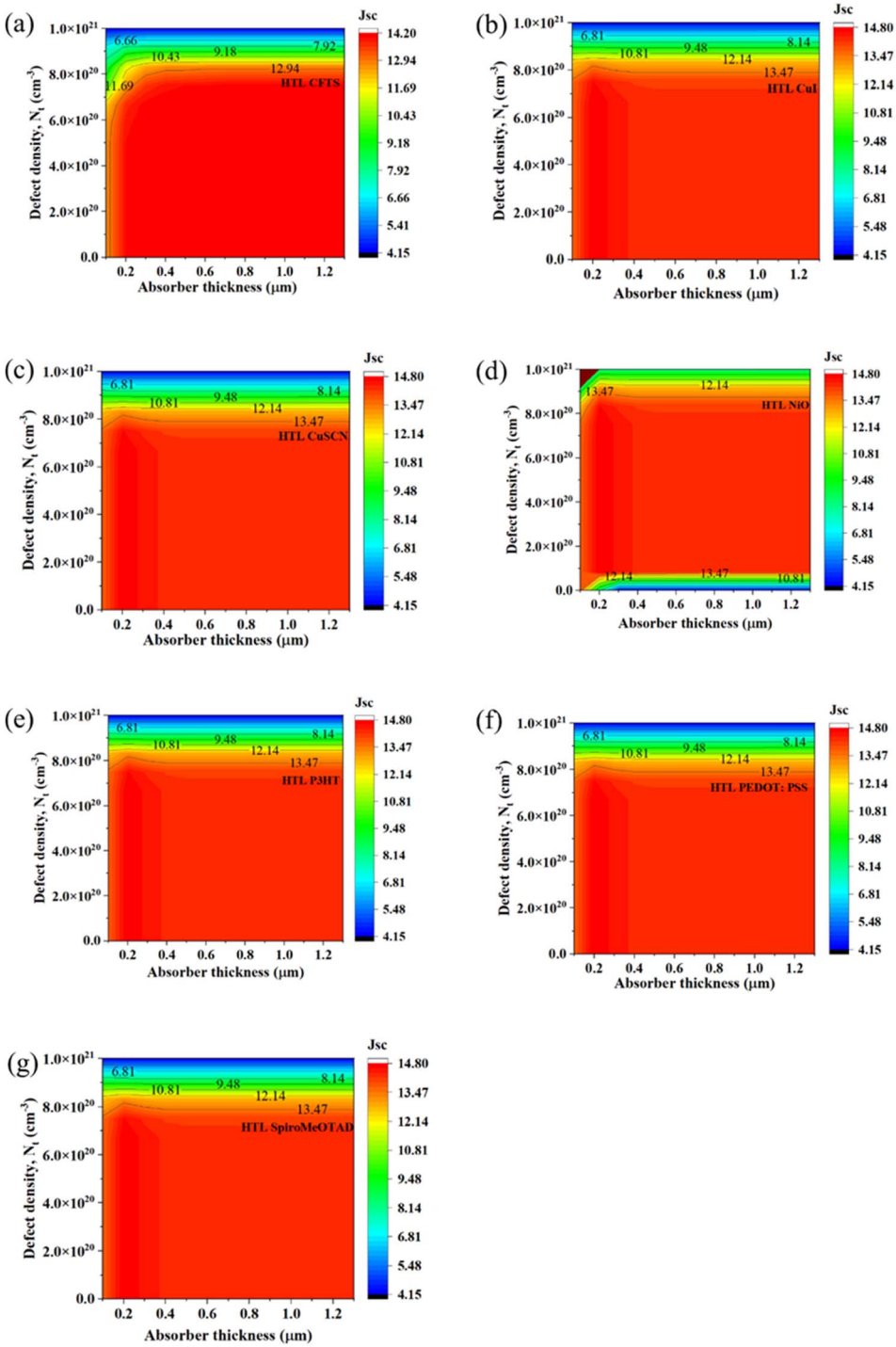

Fig. 7 (a)–(g) Contour graphs of the dependency of the J_{SC} of PSCs with different HTLs on the defect density and thickness of the PAL.

Open Access Article. Published on 04 August 2023. Downloaded on 2/24/2026 8:13:02 PM.
This article is licensed under a Creative Commons Attribution-NonCommercial 3.0 Unported Licence.

architecture. Fig. 6–9 illustrate the changes in PV characteristics, including V_{OC}, J_{SC}, FF, and PCE, of the solar cell with the variation of absorber layer defect density (N_t) and thickness. The thickness of the absorber layer was varied from 100 nm to 1300 nm, and N_t was varied from 1.0×10^9 cm^{-3} to 1.0×10^{21} cm^{-3}. The dependency of V_{OC} of the ITO/PCBM/$CsSnI_3$/CFTS/Se device was the lowest of all structures, as shown in Fig. 6(a). From the graph, it can be seen that its V_{OC} varied from 0.845 V to 0.909 V. Though it seems like its V_{OC} is almost independent of the thickness of the absorber, at $N_t > 8.0 \times 10^{20}$ cm^{-3}, V_{OC} gradually decreased from 0.909 V to 0.845 V. The dependency of V_{OC} for the rest of the studied devices ITO/PCBM/$CsSnI_3$/HTL/Se is shown in Fig. 6(b)–(f). From the graphs, it can be seen that their V_{OC} varied from 0.845 V to 0.916 V. The V_{OC} values seemed to be almost independent of the thickness of the absorber. However, at defect

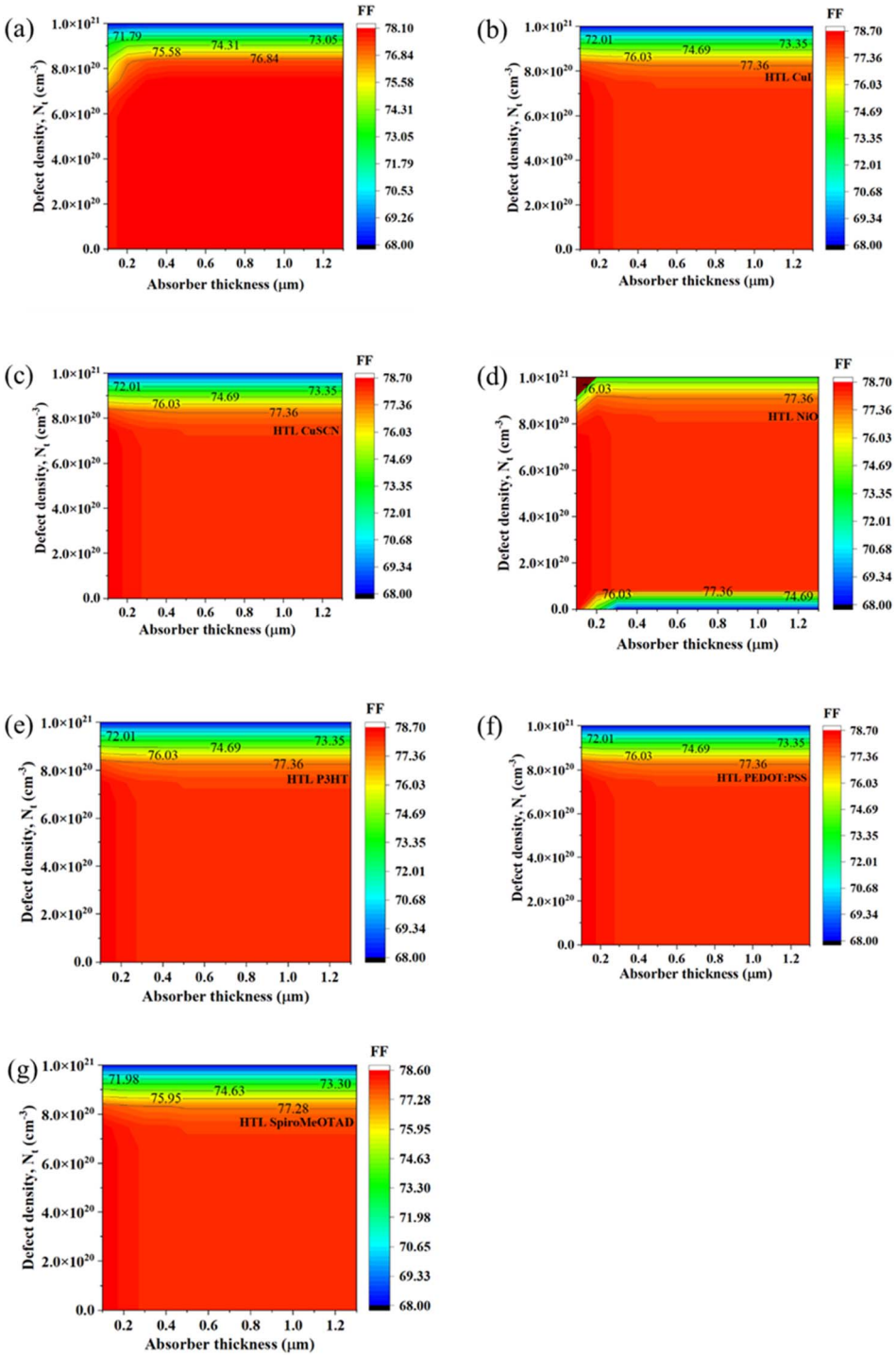

Fig. 8 (a)–(g) Contour graphs of the dependency of the FF of PSCs with different HTLs on the defect density and thickness of the PAL.

© 2023 The Author(s). Published by the Royal Society of Chemistry

Open Access Article. Published on 04 August 2023. Downloaded on 2/24/2026 8:13:02 PM.
This article is licensed under a Creative Commons Attribution-NonCommercial 3.0 Unported Licence.

density >8.0 × 10^{20} cm^{-3}, V_{OC} gradually decreased from 0.916 V to 0.845 V.

The dependency of J_{SC} of the ITO/PCBM/$CsSnI_3$/CFTS/Se device was the least among all the tested devices, as depicted in Fig. 7(a). From the graph, it can be seen that its J_{SC} varied from 4.15 mA cm^{-2} to 14.20 mA cm^{-2}. Although it seems like its J_{SC} is almost independent of the thickness of the absorber, at N_t > 7.5 × 10^{20} cm^{-3}, J_{SC} gradually decreased from 14.20 mA cm^{-2} to 4.15 mA cm^{-2}. On the other hand, the dependency of the J_{SC} of the rest of the studied devices ITO/PCBM/$CsSnI_3$/HTL/Se was higher, as shown in Fig. 7(b)–(f). From the graphs, it can be seen that J_{SC} varied from 4.15 mA cm^{-2} to 14.80 mA cm^{-2}. Their J_{SC} values seemed to be almost independent of the thickness of the absorber. However, at N_t > 8.0 × 10^{20} cm^{-3}, J_{SC} gradually decreased from 12.14 mA cm^{-2} to 4.15 mA cm^{-2}. At lower N_t, all the studied devices displayed better J_{SC}.

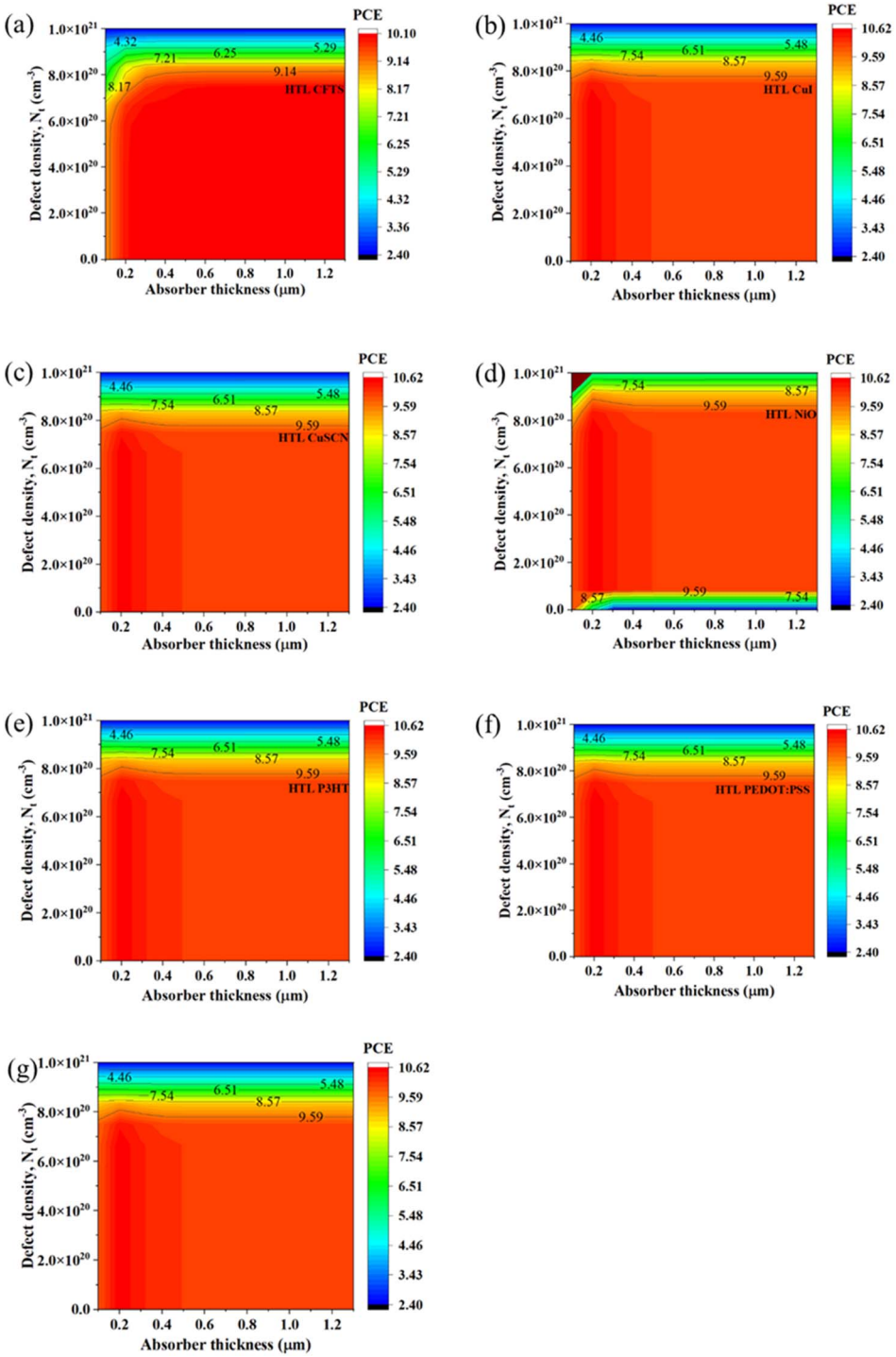

Fig. 9 (a)–(g) Contour graphs of the dependency of the PCE of PSCs with different HTLs on the defect density and thickness of the PAL.

Open Access Article. Published on 04 August 2023. Downloaded on 2/24/2026 8:13:02 PM. This article is licensed under a Creative Commons Attribution-NonCommercial 3.0 Unported Licence.

The dependency of FF of the ITO/PCBM/$CsSnI_3$/CFTS/Se device was the lowest of all, as shown in Fig. 8(a). From the graph, it can be seen that FF varied from 68.00% to 78.10%. It seems like its FF is almost independent of the thickness of the absorber. However, at $N_t > 8.0 \times 10^{20}$ cm^{-3}, FF gradually decreased from 78.10% to 68.00%. On the contrary, the dependency of FF for the rest of the studied devices ITO/PCBM/$CsSnI_3$/HTL/Se was higher, as shown in Fig. 8(b)–(f). From the graphs, it can be seen that their FF varied from 68.00% to 78.70%. Their FF values seemed to be almost independent of the thickness of the absorber. However, at $N_t > 8.0 \times 10^{20}$ cm^{-3}, FF gradually decreased from 78.70% to 68.00%.

The dependency of PCE of the ITO/PCBM/$CsSnI_3$/CFTS/Se device is shown in Fig. 9(a). From the graph, it can be seen that PCE varied from 2.40% to 10.10%. It seems like its PCE is almost independent of the thickness of the absorber. However, at $N_t > 8.0 \times 10^{20}$ cm^{-3}, PCE gradually decreased from 10.10% to 2.40%. On the contrary, the dependency of PCE for the rest of the studied devices ITO/PCBM/$CsSnI_3$/HTL/Se was higher, as presented in Fig. 9(b)–(f). For all the structures, it is evident that the PCE varied from 2.40% to 10.62%. It seemed like their PCE values were almost independent of the thickness of the absorber. However, at $N_t > 8.0 \times 10^{20}$ cm^{-3}, PCE gradually decreased from 10.62% to 2.40%.

3.3 The influence of the back metal work function

The choice of back metal contact (BMC) plays a crucial role in the performance of PSCs. In this regard, a detailed investigation was carried out to determine the impact of different BMCs on the efficiency of the PSC. Initially, different metals were used as the back metal contact (BMC) in the simulation to optimize the performance of the structures. Table 3 depicts the work functions (WFs) of the different BMCs used in the optimization study. From this study, it was seen that the efficiency of the different back contacts increased with the increase in the WF of the structure. This is because the Schottky barrier vanishes when the WF is increased to the Fermi level of the studied HTL.[62] The lowest efficiency was achieved for silver (Ag) as the back contact because it presented a lower metal WF than others. On the contrary, almost all BMCs, including when carbon (C), nickel (Ni), tungsten (W), gold (Au), platinum (Pt), and palladium (Pd), resulted in improved PV features (Table S1 in the ESI†). Based on the availability, higher WF, and performance, selenium (Se) was chosen as the optimum BMC, and the ITO/PCBM/$CsSnI_3$/HTL/Se configuration was used for further optimization of PAL, ETL, and HTL in this study.

3.4 Optimization of PAL, ETL, and HTL thickness

The optimization of the thickness of the PAL, ETL, and HTL is critical for achieving high efficiency in PSCs. The thickness of these layers can significantly affect the absorption and collection of light, charge transport, and recombination, which ultimately determine the device performance. In this section, we present the results of the optimization of PAL, ETL, and HTL thickness aimed at achieving maximum device efficiency.

Table 3 The operational WFs of the studied BMCs.[62]

Back metal contacts	Cu	Ag	Fe	C	Au	W	Ni	Pd	Pt	Se
Work function (eV)	4.65	4.26	4.81	5	5.1	5.22	5.5	5.6	5.7	5.9

3.4.1 Optimization of the absorber layer thickness. In this study, the absorber layer thickness was changed from 50 nm to 1300 nm to observe the changes in PV parameters, while the thicknesses of ETL and HTL were fixed at their initial values, as mentioned in Tables 1 and 2. As presented in Fig. 10(a), changes in PV parameters were observed with the variation of the absorber layer thickness.

For the ITO/PCBM/$CsSnI_3$/CuSCN/Se device, when the PAL thickness was increased, V_{OC} dropped from 0.918 V to 0.909 V. Moreover, J_{SC} increased initially from 10.39 mA cm^{-2} to 14.84 mA cm^{-2} and then decreased slightly to 14.24 mA cm^{-2}. Identically, with increasing PAL thickness, FF first increased from 77.50% to 78.68% and then decreased to 78.11%, and PCE also increased from 7.39% to 10.61% and further declined to 10.11%. Similarly, the devices ITO/PCBM/$CsSnI_3$/NiO/Se, ITO/PCBM/$CsSnI_3$/P3HT/Se, ITO/PCBM/$CsSnI_3$/PEDOT:PSS/Se, ITO/PCBM/$CsSnI_3$/Spiro-MeOTAD/Se, ITO/PCBM/$CsSnI_3$/CuI/Se also presented similar trends of PV parameters with an increase in PAL thickness. Because the highest efficiency was obtained at 200 nm, we considered this as the optimum thickness for the simulated PSC structures.

On the other hand, for the device ITO/PCBM/$CsSnI_3$/CFTS/Se, as PAL thickness increased, V_{OC}, J_{SC}, and FF increased from 0.903 V to 0.909 V, 10.53 mA cm^{-2} to 14.24 mA cm^{-2}, and 76.91% to 78.11%, respectively. Although the PCE of the device also increased initially from 7.32% to 10.11%, it stabilized at 10.11% with a further increase in absorber layer thickness. Since the maximum efficiency was observed at 1000 nm, it was taken as the optimum thickness for the next steps of optimization. The increment of all these parameters happens due to the increase in the photon capturing ability with the $CsSnI_3$ absorber thickness,[63] and then, the values tend to decrease with a further increment in absorber layer thickness. At a certain point, they almost stabilize at a fixed value because of the increase in recombination charge carrier and pathway resistance. For the optimum efficiency of the device, the absorber thickness should match the diffusion length of the charge carrier. After the simulation, based on the PCE, the optimum thickness of the absorber layer was taken as 1000 nm when CFTS is used as HTL and for other HTLs, the value was 200 nm.

3.4.2 Optimization of the ETL layer thickness. Fig. 10(b) depicts the change in PV features observed when ETL thickness was varied from 10 nm to 500 nm, while other parameters remained constant, and the thickness of the PAL was taken into account based on the above observations for the corresponding HTLs. For the device of ITO/PCBM/$CsSnI_3$/CuSCN/Se, while the ETL thickness increased, V_{OC} decreased from 0.913 V to 0.899 V, whereas, the other three parameters, *i.e.* J_{SC}, FF, and PCE, decreased from 14.68 mA cm^{-2} to 8.12 mA cm^{-2}, 82.14% to 81.47%, and 10.68% to 5.95%, accordingly. Similarly, the ITO/PCBM/$CsSnI_3$/NiO/Se, ITO/PCBM/$CsSnI_3$/P3HT/Se, ITO/PCBM/$CsSnI_3$/PEDOT:PSS/Se and ITO/PCBM/$CsSnI_3$/Spiro-MeOTAD/Se structures also showed a relatively similar trend of PV features.

© 2023 The Author(s). Published by the Royal Society of Chemistry

Open Access Article. Published on 04 August 2023. Downloaded on 2/24/2026 8:13:02 PM.
This article is licensed under a Creative Commons Attribution-NonCommercial 3.0 Unported Licence.

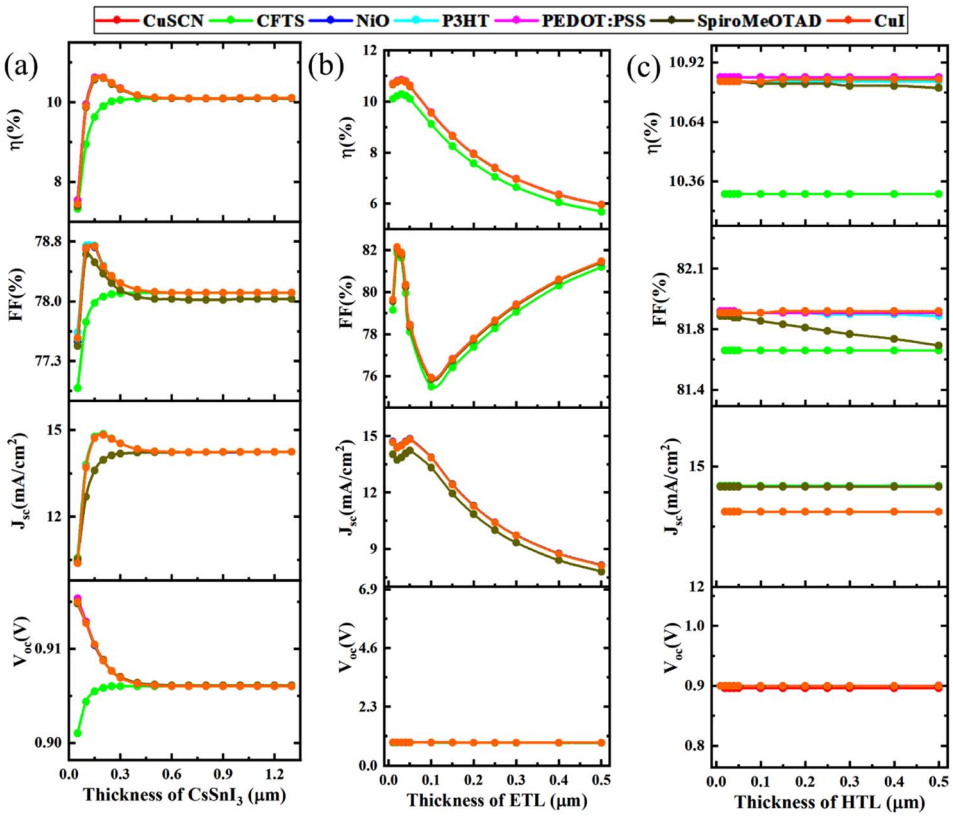

Fig. 10 The impact of variations in the (a) thickness of PAL, (b) thickness of ETL, and (c) thickness of HTL on the performance parameters of the PSCs.

Because the highest efficiency was attained at 30 nm, it was chosen as the optimum ETL thickness for these structures. For the ITO/PCBM/$CsSnI_3$/CuI/Se and ITO/PCBM/$CsSnI_3$/CFTS/Se devices, V_{OC}, J_{SC}, and FF decreased with the increase in ETL thickness. However, PCE increased initially in both structures and declined after a while. The values of V_{OC} and J_{SC} decreased with the increase in ETL layer thickness. This decrease may be because of the reduction in charge collection and generation.[43] The FF showed some decline with an increment in the thickness of the ETL layer because the series resistance increases with the increase in ETL thickness.[64] The efficiency of the solar cell increased until the thickness reached 30 nm; then, it is gradually reduced with the increment of the thickness of the ETL layer. The primary reason behind this decline with the increase in ETL layer thickness is the generation of large pinholes and uneven surfaces and also an increment in electron–hole pair recombination, which results in rising series resistance (R_S).[65]

3.4.3 Optimization of the HTL layer thickness. The impact of the thickness of HTL on the efficiency of PSC ($CsSnI_3$) is illustrated in Fig. 10(c). The thickness was varied from 10 to 500 nm to identify the optimum thickness of HTL, while the thickness of ETL was fixed at 30 nm. However, it seemed like V_{OC}, J_{SC}, FF, and PCE were not dependent on the thickness of HTL as the graph was flat for most of the HTLs; this is because inorganic HTLs have high hole mobility and conductivity.[43] Only Spiro-MeOTAD showed a little change in V_{OC}, J_{SC}, FF, and PCE. Its V_{OC} increased from 0.913 V to 0.9128 V, J_{SC} dropped to 14.493 mA cm^{-2} from 14.495 mA cm^{-2}, FF dropped from 81.85% to 81.67% and PCE also decreased from 10.83% to 10.80% due to low conductivity and low carrier mobility, which increase the layer resistivity with increasing HTL layer thickness.[43] To avoid recombination, the thickness of the HTL should be greater than the ETL.[66] As the optimized thickness of ETL is 30 nm, the optimum thickness for all HTLs was chosen as 50 nm.

3.5 Optimization of the PAL properties

3.5.1 Optimization of the PAL acceptor density. The N_A was varied from 10^9 cm^{-3} to 10^{22} cm^{-3} to observe how it affects the PV parameters of the device and find out the optimum N_A for the absorber, while the other parameters of the absorber layer, ETL, and HTL remained unchanged. Fig. 11(a) illustrates the change in V_{OC}, J_{SC}, FF, and PCE with the variation of N_A in the absorber in devices with different HTLs.

For the ITO/PCBM/$CsSnI_3$/CuSCN/Se device, with increasing N_A in the PAL, V_{OC} increased from 0.898 V to 0.955 V, J_{SC} increased from 24.33 mA cm^{-2} to 24.70 mA cm^{-2} and then dropped to 2.53 mA cm^{-2} with a further increase N_A, FF increased initially from 80.87% to 82.29% and then dropped to 81.04%, and PCE also increased from 17.68% to 17.79% and later dropped to 1.96%. The ITO/PCBM/$CsSnI_3$/P3HT/Se, ITO/PCBM/$CsSnI_3$/PEDOT:PSS/Se, ITO/PCBM/$CsSnI_3$/Spiro-MeOTAD/Se, ITO/PCBM/$CsSnI_3$/CuI/Se, and ITO/PCBM/$CsSnI_3$/CFTS/Se structures also showed a similar trend in performance. Considering the highest

Open Access Article. Published on 04 August 2023. Downloaded on 2/24/2026 8:13:02 PM. This article is licensed under a Creative Commons Attribution-NonCommercial 3.0 Unported Licence.

efficiency, the optimum N_A in the absorber layer was decided as 10^{18} cm^{-3} for all HTLs except the CFTS HTL. On the contrary, while increasing the N_A of the absorber, the ITO/PCBM/$CsSnI_3$/NiO/Se structure showed an increase in V_{OC} from 0.903 V to 0.927 V and a decrease in J_{SC} from 24.63 mA cm^{-2} to 5.56 mA cm^{-2}, while FF increases from 79.97% to 82.3% and then dropped to 81.93%, and PCE decreased from 17.8% to 4.22%. Considering the maximum efficiency, the optimum N_A of the absorber layer is determined as 10^{18} cm^{-3} while NiO is used as HTL.

V_{OC} increased with the increase in N_A because when N_A increases, the Fermi energy level drops, which results in a V_{OC} rise.[67] In the case of most HTLs, PV features like J_{SC}, FF, and PCE tended to increase gradually till 10^{18} cm^{-3}, and then, the values dropped. Because more electric field is generated with the increase in N_A, it also causes the recombination of charge carriers. While CFTS was used as the HTL, the optimum value of 10^{17} cm^{-3} was considered, for which the best improvement in efficiency from 10.30% to 24.28% was achieved. For all the other HTLs, the optimum value of N_A was 10^{18} cm^{-3}. However, CFTS provided the best efficiency because of the better band alignment between the HOMOs of CFTS and $CsSnI_3$.[43]

3.5.2 Optimization of the PAL defect density. Fig. 11(b) illustrates the change in performance parameters with the variation of the total defect density (N_t) of the PAL. To get the optimum efficiency, N_t was varied from 10^9 cm^{-3} to 10^{20} cm^{-3}, and the variation in PV parameters was observed while the other parameters remained unchanged.

For the ITO/PCBM/$CsSnI_3$/CuSCN/Se device, with the increase in absorber layer N_t, V_{OC} decreased from 0.904 V to 0.764 V, J_{SC} decreased from 24.63 mA cm^{-2} to 12.16 mA cm^{-2}, FF decreased from 79.95% to 63.52% and PCE also decreased from 17.79% to 5.9%. The ITO/PCBM/$CsSnI_3$/NiO/Se, ITO/PCBM/$CsSnI_3$/P3HT/Se, ITO/PCBM/$CsSnI_3$/PEDOT:PSS/Se, ITO/PCBM/$CsSnI_3$/Spiro-MeOTAD/Se, ITO/PCBM/$CsSnI_3$/CuI/Se, and ITO/PCBM/$CsSnI_3$/CFTS/Se structures displayed a similar kind of decline in PV performance with the increase in absorber layer N_t. The optimum absorber layer N_t was taken as 10^{15} cm^{-3} for all the structures except the case of CFTS as the HTL, for which an N_t of 10^{13} cm^{-3} was considered.

The values of V_{OC}, J_{SC}, FF, and PCE remained constant till an N_t of 10^{13} cm^{-3} when CFTS was used as the HTL, and for all other HTLs, they were constant till the N_t value of 10^{15} cm^{-3} and decreased with a further increase in absorber layer N_t, which is similar to the previous studies.[68] Therefore, these values are taken as the best optimum absorber layer N_t. The reason behind this decline in PV parameters at higher absorber layer N_t is carrier recombination, which leads to

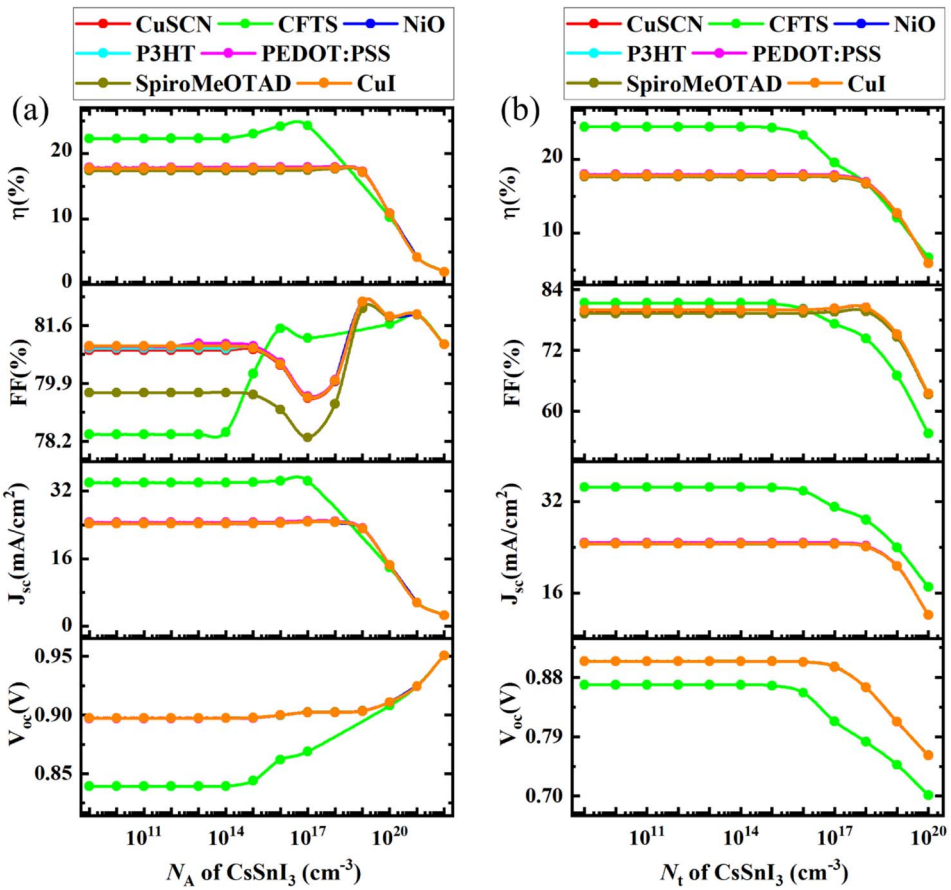

Fig. 11 (a) The influence of changes in the acceptor density in the absorber on the performance parameters, and (b) the influence of the defect density in the absorber on the performance parameters.

© 2023 The Author(s). Published by the Royal Society of Chemistry

Open Access Article. Published on 04 August 2023. Downloaded on 2/24/2026 8:13:02 PM. This article is licensed under a Creative Commons Attribution-NonCommercial 3.0 Unported Licence.

lifetime reduction and thereby reduced device performance.[63] The maximum efficiency was achieved at a lower defect density as well, but we could not consider it as the optimum value as it is nearly impossible to experimentally synthesize a material with such a small N_t.[67]

3.6 Optimization of the ETL properties

3.6.1 Optimization of the ETL layer donor density. Fig. 12(a) illustrates the changes in V_{OC}, J_{SC}, FF, and PCE with the variation of the donor density N_D in the ETL. To get the optimum efficiency, the value of ETL (PCBM) donor density was varied from 10^{11} cm^{-3} to 10^{23} cm^{-3}.

In the simulation of the device structure ITO/PCBM/$CsSnI_3$/CuSCN/Se, while on increasing the N_D value of the ETL, V_{OC} increased from 0.903 V to 0.911 V, J_{SC} decreased from 24.63 mA cm^{-2} to 22.82 mA cm^{-2}, FF increased from 80.79% to 87.01% and PCE increased from 17.98% to 18.09%. The ITO/PCBM/$CsSnI_3$/NiO/Se, ITO/PCBM/$CsSnI_3$/P3HT/Se, ITO/PCBM/$CsSnI_3$/PEDOT:PSS/Se, ITO/PCBM/$CsSnI_3$/Spiro-MeOTAD/Se, ITO/PCBM/$CsSnI_3$/CuI/Se, and ITO/PCBM/$CsSnI_3$/CFTS/Se devices also showed an increase in V_{OC}, FF, and PC*E*, while J_{SC} declined for all the combinations. Based on the results, the optimum N_D of ETL PCBM was taken as 10^{17}, 10^{15}, 10^{14}, 10^{15}, 10^{15}, 10^{15}, and 10^{18} cm^{-3}, which resulted in the maximum performance of the respective structures.

The V_{OC}, FF, and PCE increase with the increase in N_D of the ETL because at higher donor density, more charge extraction and transportation occur at the ETL/perovskite interfaces, and at lower values of N_D, these parameters are low because of series resistance.[69,70] The J_{SC} tended to decrease after a certain value of donor density of the ETL. Therefore, we chose the value of N_D as close as possible to the reference work given in Table 1 with better efficiency.

3.6.2 Optimization of the ETL layer defect density. To understand the influence of the N_t of the ETL layer on the V_{OC}, J_{SC}, FF, and PCE of the PSC, the value of N_t was varied from 10^{11} cm^{-3} to 10^{17} cm^{-3}, as illustrated in Fig. 12(b).

For the device of ITO/PCBM/$CsSnI_3$/CuSCN/Se, while increasing the defect density of the ETL, V_{OC} decreased slightly, J_{SC} decreased from 24.64 mA cm^{-2} to 24.56 mA cm^{-2}, FF decreased from 80.47% to 78.98% and PCE decreased from 17.91% to 17.52%. Similarly, the ITO/PCBM/$CsSnI_3$/NiO/Se, ITO/PCBM/$CsSnI_3$/P3HT/Se, ITO/PCBM/$CsSnI_3$/PEDOT:PSS/Se, ITO/PCBM/$CsSnI_3$/Spiro-MeOTAD/Se, ITO/PCBM/$CsSnI_3$/CuI/Se, and ITO/PCBM/$CsSnI_3$/CFTS/Se devices tended to decline in PV performance. The optimum N_t for the ETL for the respective devices were 10^{14}, 10^{14}, 10^{15}, 10^{14}, 10^{14}, 10^{14} and 10^{15}

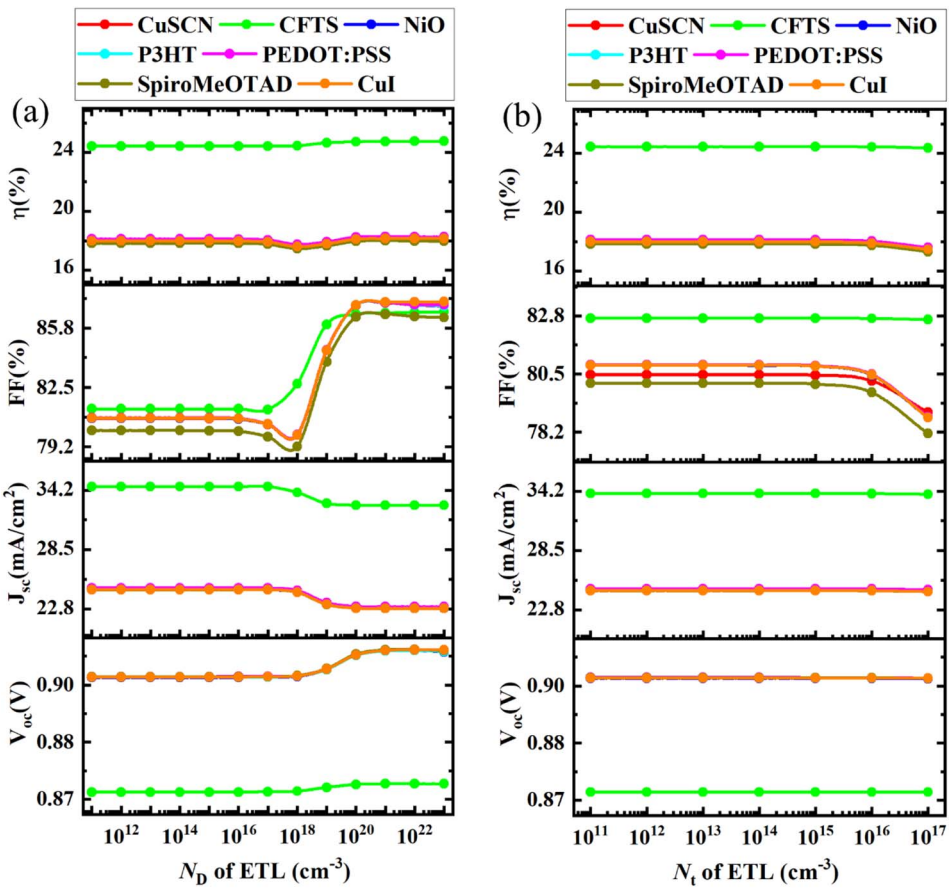

Fig. 12 (a) The influence of changes in the donor density in the ETL on the performance parameters, and (b) the influence of changes in the defect density in the ETL on the performance parameters.

Open Access Article. Published on 04 August 2023. Downloaded on 2/24/2026 8:13:02 PM. This article is licensed under a Creative Commons Attribution-NonCommercial 3.0 Unported Licence.

cm^{-3}, accordingly. It can be seen that there was not much change in the electrical parameters with the variation of the ETL layer defect density. However, the V_{OC}, J_{SC}, FF, and PCE values tended to decrease after the value of defect density reached 10^{15} cm^{-3}. This is maybe because of the recombination of charge carriers.[63] For CFTS and P3HT, the maximum values of ETL defect density remained at the initial values, while for the other HTLs used, the value of 10^{14} cm^{-3} was considered it is closer to their initial values.

3.7 Optimization of the HTL properties

3.7.1 Optimization of the HTL acceptor density. Fig. 13(a) illustrates the change in V_{OC}, J_{SC}, FF, and PCE with the variation of the N_A of the HTL. The value of N_A of the HTLs was varied from 10^{11} cm^{-3} to 10^{20} cm^{-3} to investigate the changes in performance parameters, while the other parameters were fixed at the optimized values from the above optimization studies.

For the device of ITO/PCBM/$CsSnI_3$/CuSCN/Se, while increasing the value of the N_A of CuSCN, V_{OC} decreased from 0.9035 V to 0.9034 V, J_{SC} increased from 24.644 mA cm^{-2} to 24.638 mA cm^{-2}, FF increased from 80.18% to 80.49%, and PCE increased from 17.85% to 17.92%. The performance of the ITO/PCBM/$CsSnI_3$/NiO/Se, ITO/PCBM/$CsSnI_3$/Spiro-MeOTAD/Se, and ITO/PCBM/$CsSnI_3$/CFTS/Se structures was very similar to this. The optimum N_A for the CuSCN, NiO, Spiro-MeOTAD, and CFTS HTLs was taken as 10^{18} cm^{-3}. On the other hand, for the ITO/PCBM/$CsSnI_3$/P3HT/Se structure, while increasing the value of the N_A of P3HT, V_{OC} decreased from 0.904 V to 0.903 V, J_{SC} decreased from 24.80 mA cm^{-2} to 24.63 mA cm^{-2}, FF increased from 80.65% to 80.81%, and PCE decreased from 18.07% to 17.98%. Moreover, the performance of ITO/PCBM/$CsSnI_3$/PEDOT:PSS/Se also showed the same trend with increasing N_A. The optimum N_A values for P3HT and PEDOT:PSS were taken as 10^{16} and 10^{15} cm^{-3}, respectively. For the device ITO/PCBM/$CsSnI_3$/CuI/Se, while increasing N_A of CuI, V_{OC} and FF remained unchanged in this range, while J_{SC} decreased marginally, and PCE decreased from 18% to 17.99%. The optimum N_A for the CuI HTL was taken as 10^{18} cm^{-3}, the same as the initial value.

Here, it seems like the change in HTL N_A did not affect the performance parameters much. However, for all the HTLs except CFTS, the value of V_{OC} decreased with the increase in N_A of the HTL, and for CFTS, the value increased from 0.868 to 0.876 V. This increment may be due to the electric potential at the HTL/perovskite interface.[71] In contrast, J_{SC}, FF, and PCE increased with the increase in N_A of the HTL because, at higher acceptor concentrations in the HTL, the conductivity increases and thus helps in collecting the charges faster due to enhanced

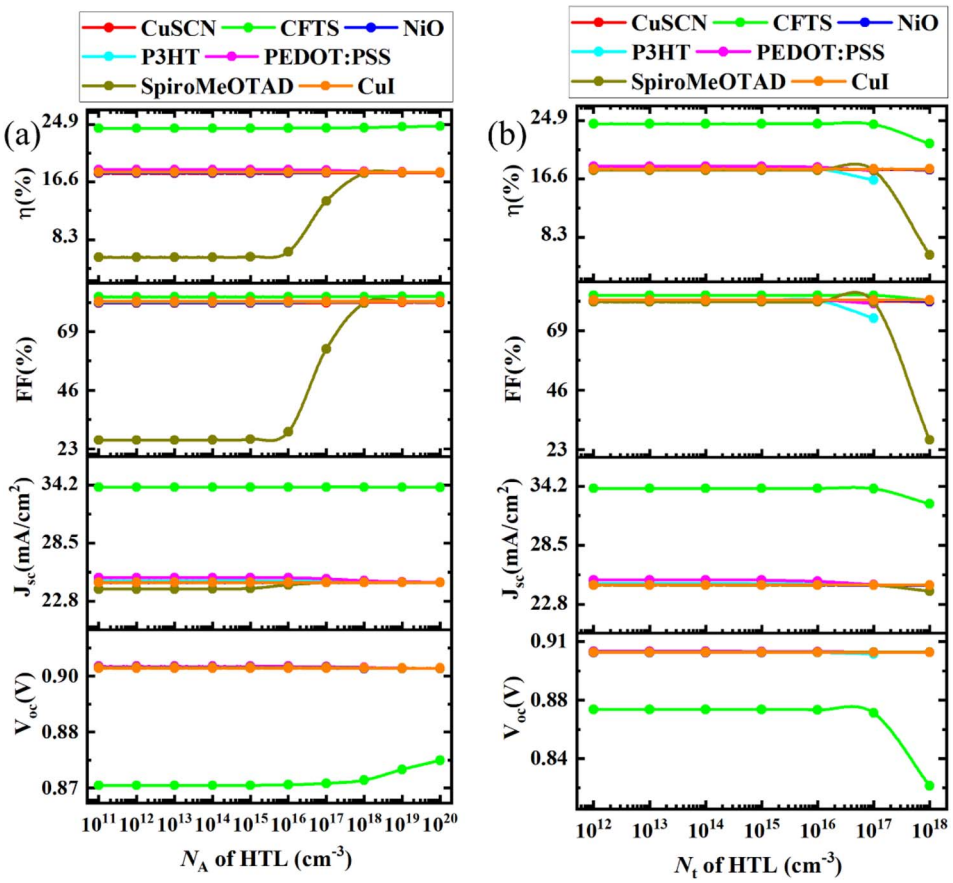

Fig. 13 (a) The influence of changes in the acceptor density in the HTL on the performance parameters, and (b) the influence of changes in the defect density in the HTL on the performance parameters.

© 2023 The Author(s). Published by the Royal Society of Chemistry

Open Access Article. Published on 04 August 2023. Downloaded on 2/24/2026 8:13:02 PM. This article is licensed under a Creative Commons Attribution-NonCommercial 3.0 Unported Licence.

electric field.[72] For P3HT and PEDOT:PSS, the optimum N_A was considered as 10^{16} cm^{-3} and 10^{15} cm^{-3}, respectively, as their performance parameters declined after these values, and for the rest of the HTLs, the optimum N_A remained the same as the initial value.

3.7.2 Optimization of the HTL defect density. The N_t of the HTL was varied from 10^{12} cm^{-3} to 10^{18} cm^{-3} to identify its influence on the V_{OC}, J_{SC}, FF, and PCE of the PSC, as illustrated in Fig. 13(b).

For the device of ITO/PCBM/$CsSnI_3$/CuSCN/Se, while increasing the N_t of CuSCN, V_{OC} increased from 0.903 V to 0.904 V, J_{SC} decreased very slightly, while FF decreased from 80.47% to 80.18% and PCE decreased from 17.91% to 17.85%. The ITO/PCBM/$CsSnI_3$/NiO/Se and ITO/PCBM/$CsSnI_3$/CFTS/Se structures performed similarly. The optimum N_t for the CuSCN, NiO, and CFTS HTLs was taken as 10^{15} cm^{-3}, which is the same as the initial value. On the contrary, for the ITO/PCBM/$CsSnI_3$/P3HT/Se and ITO/PCBM/$CsSnI_3$/PEDOT:PSS/Se structures, while increasing the N_t of P3HT and PEDOT:PSS, V_{OC} decreased from 0.904 V to 0.903 V (almost unchanged), while J_{SC}, FF, and PCE decreased as well like the other structures. The optimum N_t for P3HT and PEDOT:PSS was taken as 10^{14} cm^{-3}, which is almost the same as the initial value.

However, for the ITO/PCBM/$CsSnI_3$/Spiro-MeOTAD/Se device, while increasing the N_t of Spiro-MeOTAD, V_{OC} remained unchanged in this range, and J_{SC}, FF, and PCE decreased similar to the other studied structures. Meanwhile, for the ITO/PCBM/$CsSnI_3$/CuI/Se device, while increasing the N_t of CuI, all the PV features like V_{OC}, J_{SC}, FF, and PCE remained unchanged within this range. The optimum N_t for Spiro-MeOTAD and CuI was taken as 10^{15} cm^{-3}, which is the same as the initial value.

The values of the PV features remain unchanged until a certain value of N_t of the HTL, and then they begin to drop with a further increment in N_t. This decline is because of carrier recombination at higher defect densities.[63] The maximum PCE was obtained at lower N_t too, but as it is nearly impossible to synthesize a material with very low N_t, we chose the close value of 10^{15} cm^{-3} as the optimum N_t, and it is the same as the initial value from Table 1.

3.8 Optimization of the interface properties

The band energy alignment of the interface energy levels of the charge transport layers and absorber material represents one of the issues that the PSC community is concerned about. To get overcome these challenges, attempts should be made to link experimental and theoretical studies. We could observe the formation of two distinct formations connected to the CBO of the ETL/$CsSnI_3$ interface by the theoretical modeling described in Section 2, which hinges on the distinction between the electron affinities of the ETL (EA_{ETL}) and the absorber ($EA_{Absorber}$). In the scenario of PCBM, the energy cliff CBO– is generated with no possible barrier for electrons, which aids in the collection mechanism, if the conduction band of the ETL is less than that of the absorber. The spike-like conformation CBO+ is produced and acts as an electron barrier, if the conduction band of the ETL is substantially high in comparison with that of the perovskite. At the perovskite/HTL interface, an optimal energy band alignment is also necessary for enhanced PSC efficiency. The valence band of the absorber layer and that of HTM differ significantly. Valence energy alignment is necessary, as already mentioned, to improve the photovoltaic characteristics. The energy diagram of the perovskite active layer, HTLs, and ETL is shown in Fig. 14. This figure remarks the suitability of CFTS, which offers a suitable band alignment that enhances the collection mechanism and establishes an efficient blocking barrier for electrons.

3.8.1 Optimization of defect density in the HTL and the $CsSnI_3$ absorber layer. Fig. 15(a) illustrates the influence of the change in the HTL/$CsSnI_3$ interface defect density, N_t, on the PV performance parameters. The value of N_t was varied from 10^{10} cm^{-2} to 10^{22} cm^{-2} to observe its effect on the performance parameters of the PSC. The values of V_{OC}, J_{SC}, FF, and PCE decreased with the increase in N_t of the HTL/$CsSnI_3$ interface for all the studied structures. The best efficiency was obtained when the value of N_t was about 10^{10} cm^{-2} Then, all the PV features of the device started to decline because of the acceleration of the recombination of the charge carriers.[68] Therefore, for all the HTLs, the optimum value of HTL/$CsSnI_3$ interface defect density was kept at the initial value of 10^{10} cm^{-2}.

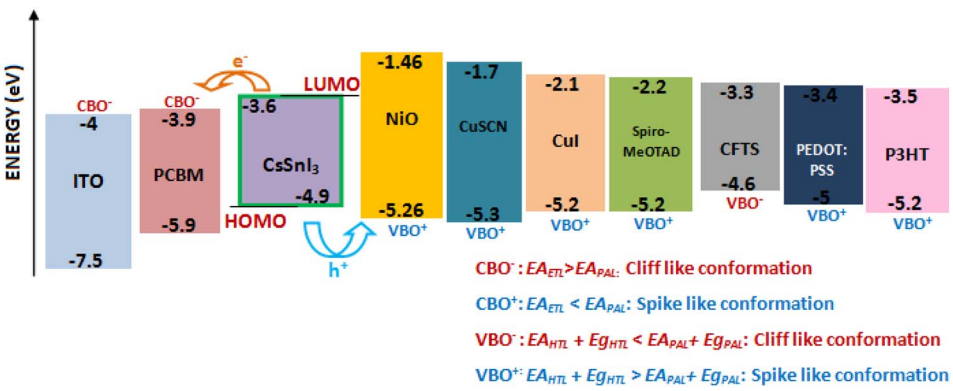

Fig. 14 The energy diagram of the perovskite active layer and the charge transport materials.

Open Access Article. Published on 04 August 2023. Downloaded on 2/24/2026 8:13:02 PM.
This article is licensed under a Creative Commons Attribution-NonCommercial 3.0 Unported Licence.

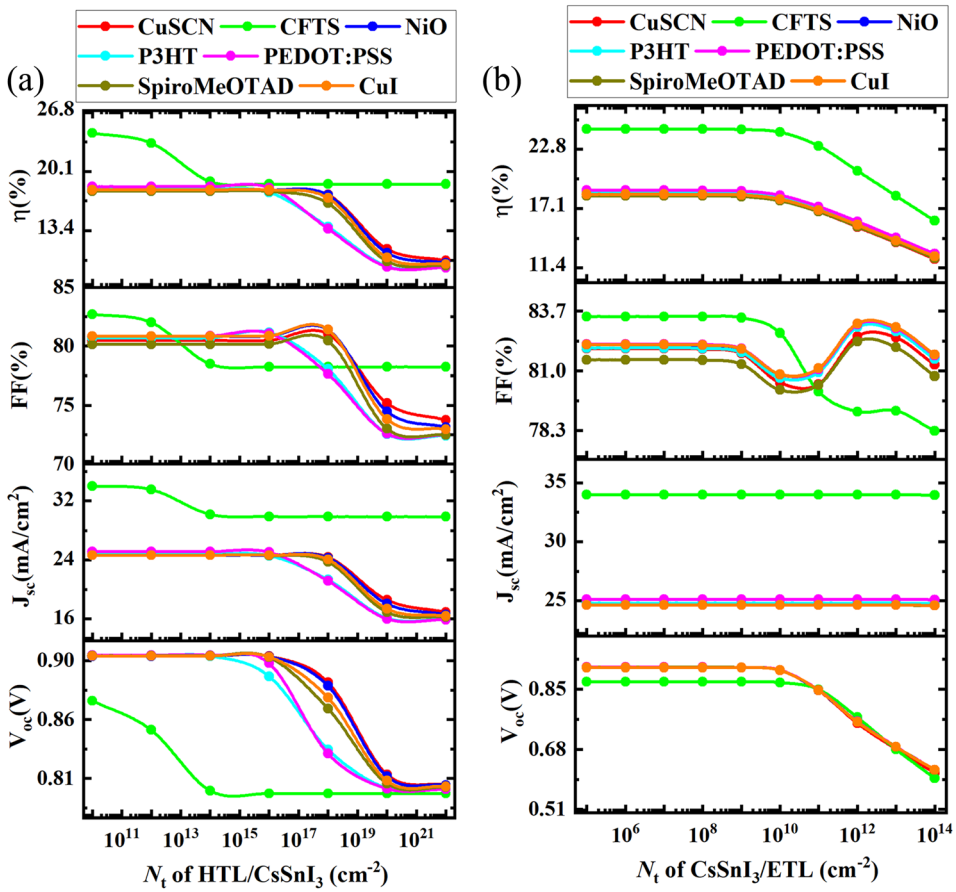

Fig. 15 (a) The effect of changes in the HTL/$CsSnI_3$ interface defect density, N_t, on the performance parameters, and (b) the effect of changes in the $CsSnI_3$/PCBM interface defect density, N_t, on the performance parameters.

3.8.2 Optimization of defect density in the $CsSnI_3$ absorber layer and the ETL PCBM. Fig. 15(b) illustrates the change in V_{OC}, J_{SC}, FF, and PCE with the variation of the $CsSnI_3$/PCBM interface defect density, N_t. To observe the variations in these performance parameters, the value of N_t was varied from 10^5 cm^{-2} to 10^{14} cm^{-2}. V_{OC}, J_{SC}, FF, and PCE remained nearly unchanged till 10^8 cm^{-2} and then, they started to decline with a further increase in defect density. This decline may be because of the higher recombination rate of the charge carriers at high values of N_t.[68] For CuSCN and CFTS, the optimum value of $CsSnI_3$/PCBM was taken as 10^8 cm^{-2}, and for the other HTLs, the value remained the same as the initial value 10^{10} cm^{-2}.

3.9 The influence of series resistance, shunt resistance, and temperature

3.9.1 The influence of series resistance. Series resistance R_S is one of the factors that are responsible for the reduction in the efficiency of the PSC. The origin of R_S is generally associated with charge transporting layers, the absorber layer, and the front and back contacts (ITO and Se). Fig. 16(a) represents the influence of changing series resistance R_S on the V_{OC}, J_{SC}, FF, and PCE of the PSC. In this work, the value of R_S was varied from 0 Ω cm^2 to 6 Ω cm^2, while the shunt resistance (R_{Sh}) was fixed at 10^5 Ω cm^2.

As seen in the figure, the values of V_{OC} and J_{SC} of all studied structures were not influenced much by the change in series resistance but the values of FF and efficiency gradually decreased with the increase in R_S. Because, whenever series resistance increases, it causes a lack of power in the solar cell, thus declining the PCE of the solar cell.

3.9.2 The influence of shunt resistance. Recombination defect states are the main sources of R_{Sh} in the solar cell. The influence of R_{Sh} on the PV parameters V_{OC}, J_{SC}, FF, and PCE is illustrated in Fig. 16(b) while the value of R_{Sh} was varied from 10 to 10^7 Ω cm^2 and R_S was fixed at 0.5 Ω cm^2.

The values of the performance parameters decreased with the increase in R_{Sh} because when the shunt resistance increases, the defect states decrease, leading to a reduction in the charge recombination rate, which increases the PCE of the solar cell.[73,74] Therefore, it is obvious that a low value of R_S and a high value of R_{Sh} are required to get a higher PCE. For an ideal solar device, the value of R_S is zero, and the value of shunt resistance is infinite, but in practice, it is impossible to implement these values.

3.9.3 The influence of temperature. The temperature of a solar cell is greater than the room temperature most of the time, and this increase in temperature plays an important role in the PV characteristics of the solar cell. To observe its impact, the temperature was varied from 275 K to 475 K, and the

© 2023 The Author(s). Published by the Royal Society of Chemistry

Open Access Article. Published on 04 August 2023. Downloaded on 2/24/2026 8:13:02 PM.
This article is licensed under a Creative Commons Attribution-NonCommercial 3.0 Unported Licence.

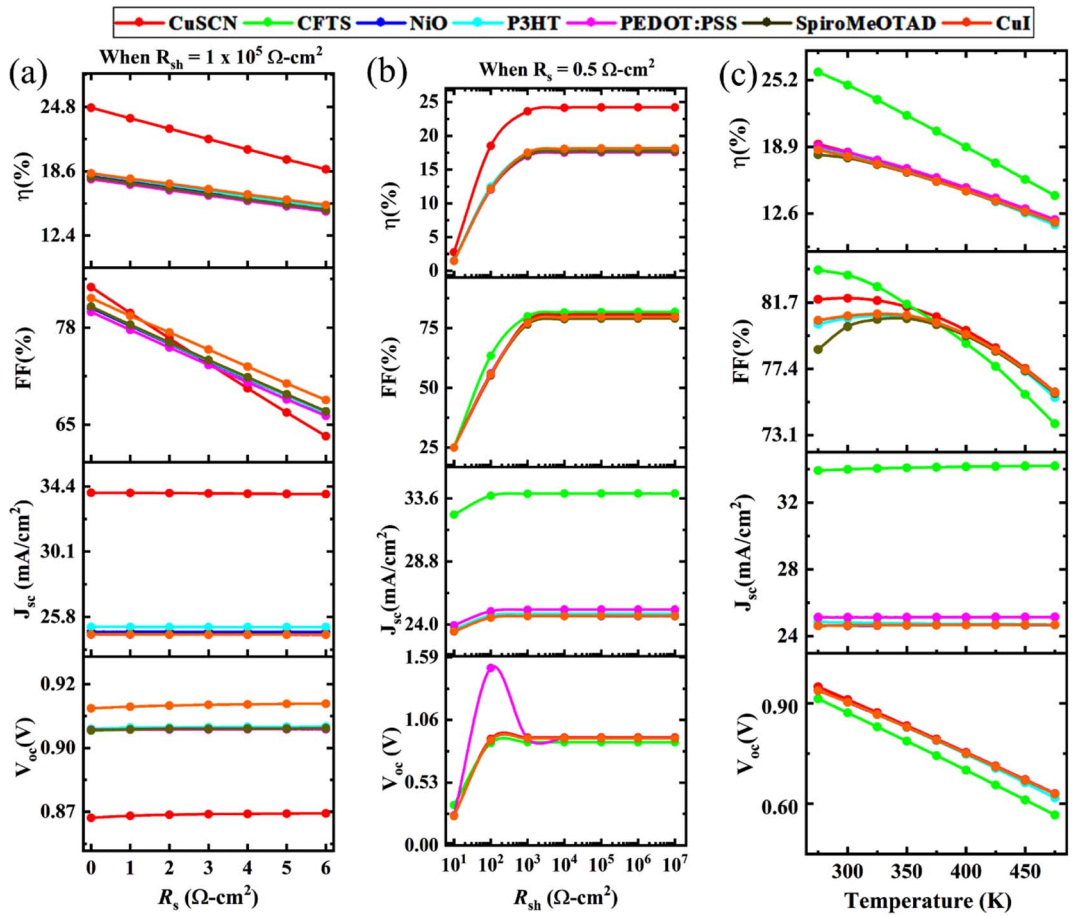

Fig. 16 The influence of changes in (a) series resistance, R_S (Ω cm^2), (b) shunt resistance, R_{Sh} (Ω cm^2), and (c) temperature (K) on the performance parameters V_{OC}, J_{SC}, FF, and PCE of PSCs.

influence of this change on V_{OC},J_{SC}, FF, and PCE is illustrated in Fig. 16(c).

Here, the V_{OC} of all structures tended to decrease with the increase in temperature because at higher temperatures, the reverse saturation current density (J_0) increases. Due to the reverse relationship between V_{OC} and J_0, V_{OC} decreases with the increase in J_0, and this is represented in eqn (6).

$$V_{oc} = \frac{AK_BT}{q}\left[\ln\left(1+\frac{J_{sc}}{J_0}\right)\right] \quad (6)$$

where A is the ideality factor, and $\frac{K_BT}{q}$ is the thermal voltage.

From the simulation, it could be seen that temperature had almost no influence on J_{SC}, but FF and PCE decreased with the increase in temperature. This decline may be due to the cutback of shunt resistance.[75] Another possible reason for this decrement in PCE might be the enhanced charged recombination rate at higher temperatures due to the drop in charge recombination resistance.

3.10 The influence of current–voltage density and quantum efficiency

3.10.1 The influence of current–voltage density. Fig. 17(a) and (b) show the change in current density with respect to voltage (J–V) for the initial and final optimized structures of ITO/PCBM/$CsSnI_3$/HTL/Se. To study the influence of different parameters on the PCE, the physical parameters were used; then, at every optimization stage, the value of the current density started to rise, and at the final stage, the highest change was for the device with CFTS, which was almost 140% of the initial value because of the good band alignment of CFTS with the $CsSnI_3$ PAL.

3.10.2 The influence of quantum efficiency. The quantum efficiency curves for the initial and final optimized devices are shown in Fig. 17(c) and (d), respectively. With every optimization, the value of QE tended to rise. While CFTS was used as the HTL, the curve was almost square-shaped, which is the ideal shape of QE for PSCs. The external quantum efficiency (EQE) *vs.* wavelength curve showed approximately 99.6% efficiency in the 620 nm–650 nm visible range when CFTS was used as the HTL.

3.11 Comparison of the SCAPS-1D results with previous work

The optimized results of the absorber layer, ETL layer, and HTL layer for the best-optimized device are listed in Table 4. Meanwhile, Table 5 represents the PV parameters from

Open Access Article. Published on 04 August 2023. Downloaded on 2/24/2026 8:13:02 PM.
This article is licensed under a Creative Commons Attribution-NonCommercial 3.0 Unported Licence.

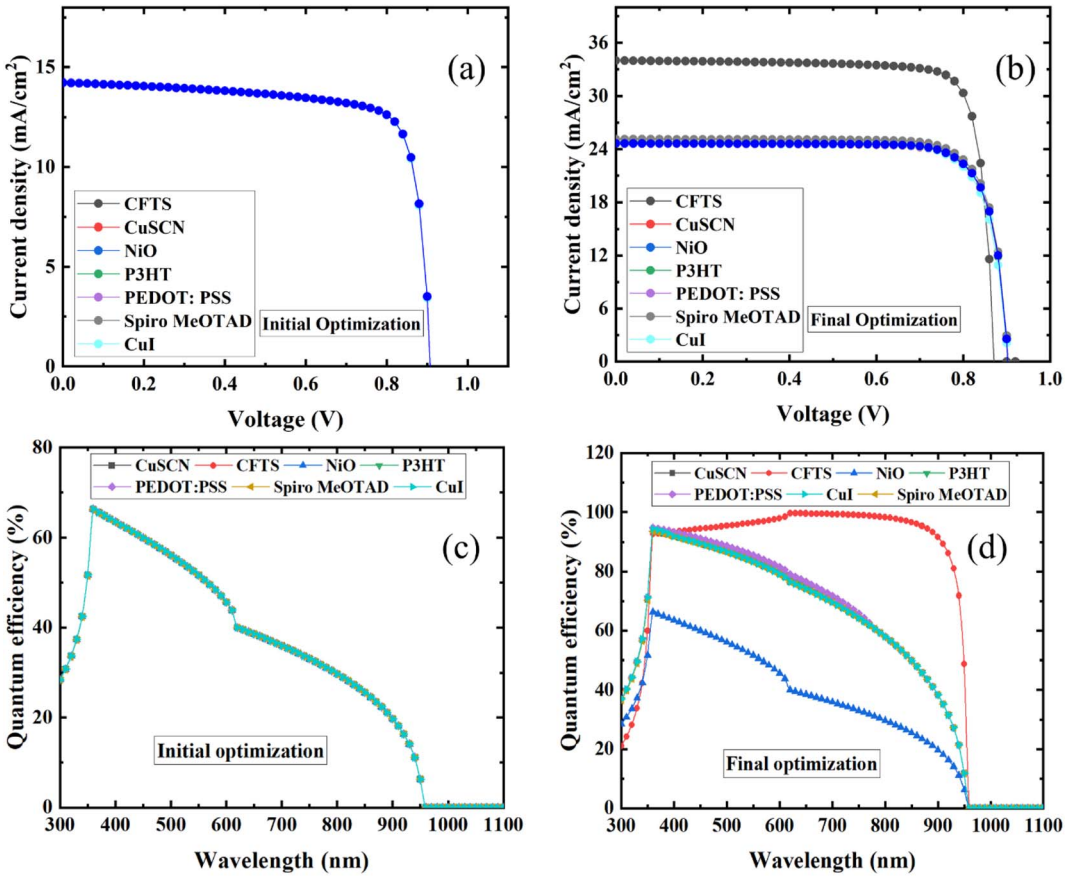

Fig. 17 (a) The current density–voltage curve for the initial optimized structure, (b) the current density–voltage curve for the final optimized structure ITO/PCBM/$CsSnI_3$/HTL/Se, (c) the QE curve of the initial optimized structure and (d) the QE curve of the final optimized structure ITO/PCBM/$CsSnI_3$/HTL/Se.

Table 4 The optimized values of the characteristic parameters of the final optimized device

Parameters	CFTS	$CsSnI_3$	PCBM
Thickness (nm)	100	1000	30
E_g (eV)	1.3	1.3	2
χ (eV)	3.3	3.6	3.9
ε_r	9	9.93	3.9
N_C (cm^{-3})	2.2×10^{18}	1×10^{19}	2.5×10^{21}
N_V (cm^{-3})	1.8×10^{19}	1×10^{18}	2.5×10^{21}
μ_n ($cm^2\ V^{-1}\ s^{-1}$)	21.98	1.5×10^3	0.2
μ_h ($cm^2\ V^{-1}\ s^{-1}$)	21.98	5.85×10^2	0.2
N_A (cm^{-3})	1×10^{18}	1×10^{20}	—
N_D (cm^{-3})	—	—	2.93×10^{17}
N_t (cm^{-3})	1.0×10^{15}	1.0×10^{13}	1.0×10^{15}

previous works (theoretical and practical studies) using $CsSnI_3$ as the absorber layer for comparison with this work. From the table, it can be seen that $CsSnI_3$ as an absorber layer couldn't provide the expected efficiency, but in the case of our optimized device, it provides greater efficiency compared with other works. Song *et al.* mixed piperazine with $CsSnI_3$ to increase its PCE but was only able to achieve an efficiency of 3.83%.[27] Chen *et al.* tried to replace the halide of $CsSnI_3$ to get a better PCE but only got a PCE of 12.96%.[16] Kumar *et al.* tried to mix SnF_2 with an absorber layer and got only 2.02% efficiency for the device.[76] Rahman *et al.* and Wang *et al.* experimentally obtained 11.41%[77] and 3.31% PCE,[78] respectively. With the optimized values from this study and our previous study,[50] we found that the PCE of our device increased from 10.11% to 24.73%, and for a Pb-free PSC, this PCE value is remarkable as this solar cell is environmentally friendly due to its inorganic charge transport layers. Regarding fabrication feasibility, most of the sandwiched architecture-based perovskite solar cells reported in the literature are fabricated using spin-coating techniques, and the same can be utilised to fabricate the optimised ITO/PCBM/$CsSnI_3$/CuSCN/Se-based solar cell. The thickness of each layer, material quality, annealing temperature, and encapsulation are important parameters to be considered when fabricating the device by spin-coating. With careful control of these parameters, it is possible to fabricate high-performance ITO/PCBM/$CsSnI_3$/CuSCN/Se devices. Besides, the optimized $CsSnI_3$ can be fabricated *via* different commonly used fabrication techniques, such as the doctor blade process, sequential deposition, hybrid chemical vapor, and alternating layer-by-layer process.[79]

© 2023 The Author(s). Published by the Royal Society of Chemistry

Open Access Article. Published on 04 August 2023. Downloaded on 2/24/2026 8:13:02 PM. This article is licensed under a Creative Commons Attribution-NonCommercial 3.0 Unported Licence.

Table 5 Comparison of previous works using $CsSnI_3$ as the absorber material and this work[a]

Type	Device structure	V_{OC} (V)	J_{SC} (mA cm^{-2})	FF (%)	PCE (%)	Ref.
1	FTO/TiO_2/$CsSnI_3$/Au	0.34	20.63	54.18	3.83	27
1	ITO/TiO_2/$CsSnI_3$/Spiro-OMeTAD/Au	0.86	23.20	65.00	12.96	16
1	FTO/TiO_2/$CsSnI_3$/*m*-MTDATA/Au	0.24	22.70	0.37	2.02	76
2	ITO/NiO_x/$CsSnI_3$/PCBM/Al	1.19	17.29	55.27	11.41	77
2	ITO/TiO_2/$MASnI_3$/Spiro-OMeTAD/Au	0.88	16.80	0.42	6.40	80
2	ITO/PCBM/$CsSnI_3$/NiO_2/Al	0.52	10.21	62.50	3.31	78
2	ITO/PCBM/$CsSnI_3$/CuI/Au	0.91	14.24	78.11	10.10	50
2	ITO/PCBM/$CsSnI_3$/CFTS/Se	0.87	33.99	83.46	24.73	[b]

[a] Note: 1- experimental, 2- theoretical. [b] This work.

4 Conclusion

In this study, we conducted simulations for the optimization of the performance of lead-free $CsSnI_3$-based solar cells with various HTLs and PCBM as the ETL. Our findings demonstrate that the optimal structure is ITO/PCBM/$CsSnI_3$/CFTS/Se, which is capable of achieving a PCE of 24.73%, along with a V_{OC} of 0.87 V, a J_{SC} of 33.99 mA cm^{-2}, and a FF of 83.46%. We also explored the influence of both series and shunt resistances on the PCE of the solar cells. Our results suggest that a smaller value of series resistance and a higher value of shunt resistance are suitable for achieving maximum efficiency. Additionally, we observed that the temperature significantly affects the PCE of the PSC, with the highest efficiency being achieved at 300 K. Furthermore, our study also reveals that the QE of solar cells is highly dependent on the choice of HTL. While using CFTS as the HTL, the QE curve showed a higher value of 99.6% in the visible range of 620 nm–650 nm. Overall, our simulations provide valuable insights into the optimization of $CsSnI_3$-based solar cells with various HTLs and PCBM ETL. These findings can potentially contribute to developing cost-effective solar cells with higher efficiency for future applications.

Data availability

The raw/processed data required to reproduce these findings cannot be shared at this time as the data also forms part of an ongoing study.

Author contributions

M. K. Hossain: conceptualization, data curation, formal analysis, funding acquisition, investigation, methodology, project administration, resources, software, supervision, validation, visualization, writing – original draft, and writing – review & editing; M. S. Uddin, G. F. I. Toki, M. K. A. Mohammed, and R. Pandey: data curation, formal analysis, investigation, software, validation, visualization, and writing – original draft; J. Madan, M. F. Rahman, M. R. Islam, S. Bhattarai, H. Bencherif, D. P. Samajdar, Mongi Amami, and D. K. Dwivedi: data curation, formal analysis, investigation, validation, visualization, and writing – review & editing.

Conflicts of interest

The authors declare that they have no known competing financial interests or personal relationships that could have appeared to influence the work reported in this paper.

Acknowledgements

The authors have extend their appreciation to the Deanship of Scientific Research at King Khalid University, Saudi Arabia for funding this work through Research Groups Program under grant number R.G.P.2:200/44. The SCAPS-1D program was kindly provided by Dr M. Burgelman of the University of Gent in Belgium. The authors would like to express their gratitude to him.

References

1 M. H. K. Rubel, M. A. Hossain, M. K. Hossain, K. M. Hossain, A. A. Khatun, M. M. Rahaman, M. Ferdous Rahman, M. M. Hossain and J. Hossain, *Results Phys.*, 2022, **42**, 105977.
2 M. R. Islam, A. A. M. Mazumder, M. R. H. Mojumder, A. S. M. Z. Shifat and M. K. Hossain, *Jpn. J. Appl. Phys.*, 2023, **62**, 011002.
3 M. K. Hossain, M. H. K. Rubel, G. F. I. Toki, I. Alam, M. F. Rahman and H. Bencherif, *ACS Omega*, 2022, **7**, 43210–43230.
4 R. Pandey, S. Bhattarai, K. Sharma, J. Madan, A. K. Al-Mousoi, M. K. A. Mohammed and M. K. Hossain, *ACS Appl. Electron. Mater.*, 2023, DOI: **10.1021/acsaelm.2c01574**.
5 H. Bencherif and M. K. Hossain, *Sol. Energy*, 2022, **248**, 137–148.
6 S. Kazim, M. K. Nazeeruddin, M. Grätzel and S. Ahmad, *Angew. Chem., Int. Ed.*, 2014, **53**, 2812–2824.
7 M. K. Hossain, A. A. Arnab, R. C. Das, K. M. Hossain, M. H. K. Rubel, M. F. Rahman, H. Bencherif, M. E. Emetere, M. K. A. Mohammed and R. Pandey, *RSC Adv.*, 2022, **12**, 34850–34873.
8 A. K. Al-Mousoi, M. K. A. Mohammed, A. Kumar, R. Pandey, J. Madan, D. Dastan, M. K. Hossain, P. Sakthivel, A. Ganesan and Z. M. Yaseen, *Phys. Chem. Chem. Phys.*, 2023, **25**, 16459–16468.

Open Access Article. Published on 04 August 2023. Downloaded on 2/24/2026 8:13:02 PM. This article is licensed under a Creative Commons Attribution-NonCommercial 3.0 Unported Licence.

9 M. H. K. Rubel, S. K. Mitro, M. K. Hossain, K. M. Hossain, M. M. Rahaman, J. Hossain, B. K. Mondal, A. Akter, M. F. Rahman, I. Ahmed and A. K. M. A. Islam, *Mater. Today Commun.*, 2022, **33**, 104302.
10 A. Kojima, K. Teshima, Y. Shirai and T. Miyasaka, *J. Am. Chem. Soc.*, 2009, **131**, 6050–6051.
11 L. Serrano-Lujan, N. Espinosa, T. T. Larsen-Olsen, J. Abad, A. Urbina and F. C. Krebs, *Adv. Energy Mater.*, 2015, **5**, 1501119.
12 S. Shao, J. Liu, G. Portale, H.-H. Fang, G. R. Blake, G. H. ten Brink, L. J. A. Koster and M. A. Loi, *Adv. Energy Mater.*, 2018, **8**, 1702019.
13 J. Wei, Q. Xiong, S. M. Mahpeykar and X. Wang, *Nanomaterials*, 2016, **6**, 55.
14 F. Hao, C. C. Stoumpos, D. H. Cao, R. P. H. Chang and M. G. Kanatzidis, *Nat. Photonics*, 2014, **8**, 489–494.
15 S. Saurabh, M. K. Hossain, S. Singh, S. K. Agnihotri and D. P. Samajdar, *RSC Adv.*, 2023, **13**, 9878–9891.
16 L.-J. Chen, C.-R. Lee, Y.-J. Chuang, Z.-H. Wu and C. Chen, *J. Phys. Chem. Lett.*, 2016, **7**, 5028–5035.
17 K. Shum, Z. Chen, J. Qureshi, C. Yu, J. J. Wang, W. Pfenninger, N. Vockic, J. Midgley and J. T. Kenney, *Appl. Phys. Lett.*, 2010, **96**, 221903.
18 Z. Chen, C. Yu, K. Shum, J. J. Wang, W. Pfenninger, N. Vockic, J. Midgley and J. T. Kenney, *J. Lumin.*, 2012, **132**, 345–349.
19 X. Meng, J. Lin, X. Liu, X. He, Y. Wang, T. Noda, T. Wu, X. Yang and L. Han, *Adv. Mater.*, 2019, **31**, 1903721.
20 Z. Zhu, N. Li, D. Zhao, L. Wang and A. K. -Y. Jen, *Adv. Energy Mater.*, 2019, **9**, 1802774.
21 Z. Zhang, Q. Sun, T. Nakajima, H. Ban, Z. Liu, H. Yu, Y. Wang, Z. Xiao, Y. Shen and M. Wang, *J. Mater. Chem. A*, 2022, **10**, 23204–23211.
22 K. P. Marshall, M. Walker, R. I. Walton and R. A. Hatton, *Nat. Energy*, 2016, **1**, 16178.
23 K. Xu, *Instrum. Sci. Technol.*, 2021, **49**, 91–105.
24 M. K. Hossain, M. K. A. Mohammed, R. Pandey, A. A. Arnab, M. H. K. Rubel, K. M. Hossain, M. H. Ali, M. F. Rahman, H. Bencherif, J. Madan, M. R. Islam, D. P. Samajdar and S. Bhattarai, *Energy Fuels*, 2023, **37**, 6078–6098.
25 M. K. Hossain, G. F. I. Toki, A. Kuddus, M. H. K. Rubel, M. M. Hossain, H. Bencherif, M. F. Rahman, M. R. Islam and M. Mushtaq, *Sci. Rep.*, 2023, **13**, 2521.
26 B. Wu, Y. Zhou, G. Xing, Q. Xu, H. F. Garces, A. Solanki, T. W. Goh, N. P. Padture and T. C. Sum, *Adv. Funct. Mater.*, 2017, **27**, 1604818.
27 T. Bin Song, T. Yokoyama, J. Logsdon, M. R. Wasielewski, S. Aramaki and M. G. Kanatzidis, *ACS Appl. Energy Mater.*, 2018, **1**, 4221–4226.
28 D. Dastan, M. K. A. Mohammed, A. K. Al-Mousoi, A. Kumar, S. Q. Salih, P. S. JosephNg, D. S. Ahmed, R. Pandey, Z. M. Yaseen and M. K. Hossain, *Sci. Rep.*, 2023, **13**, 9076.
29 M. K. Basher, S. M. Shah Riyadh, M. K. Hossain, M. Hassan, M. A. R. Akand, S. M. Amir-Al Zumahi, M. A. Matin, N. Das and M. Nur-E-Alam, *Opt. Quantum Electron.*, 2023, **55**, 322.
30 M. K. A. Mohammed, A. K. Al-Mousoi, A. Kumar, A. R. J. Katae, O. A. Khaleel, D. S. Ahmed and M. K. Hossain, *J. Mater. Sci.*, 2023, **58**, 11748–11760.
31 A. Thakur, D. Singh and S. Kaur Gill, *Mater. Today: Proc.*, 2022, **71**, 195–201.
32 T. Dureja, A. Garg, S. Bhalla, D. Bhutani and A. Khanna, *Mater. Today: Proc.*, 2022, **71**, 239–242.
33 Y. Miyamoto, S. Kusumoto, T. Yokoyama, Y. Nishitani, T. Matsui, T. Kouzaki, R. Nishikubo, A. Saeki and Y. Kaneko, *ACS Appl. Nano Mater.*, 2020, **3**, 11650–11657.
34 N. Shrivastav, S. Kashyap, J. Madan, M. K. A. Mohammed, M. K. Hossain and R. Pandey, *Optik*, 2023, **281**, 170821.
35 Y. Bai, H. Yu, Z. Zhu, K. Jiang, T. Zhang, N. Zhao, S. Yang and H. Yan, *J. Mater. Chem. A*, 2015, **3**, 9098–9102.
36 Z. Zhang, M. Sheri, Z. A. Page, T. Emrick, A. Saeki, Y. Liu and T. P. Russell, *ACS Appl. Mater. Interfaces*, 2020, **12**, 56068–56075.
37 S. Li, Y.-L. Cao, W.-H. Li and Z.-S. Bo, *Rare Met.*, 2021, **40**, 2712–2729.
38 W. Liao, D. Zhao, Y. Yu, C. R. Grice, C. Wang, A. J. Cimaroli, P. Schulz, W. Meng, K. Zhu, R. Xiong and Y. Yan, *Adv. Mater.*, 2016, **28**, 9333–9340.
39 L. Xu, X. Feng, W. Jia, W. Lv, A. Mei, Y. Zhou, Q. Zhang, R. Chen and W. Huang, *Energy Environ. Sci.*, 2021, **14**, 4292–4317.
40 M. K. Hossain, G. F. Ishraque Toki, D. P. Samajdar, M. H. K. Rubel, M. Mushtaq, M. R. Islam, M. F. Rahman, S. Bhattarai, H. Bencherif, M. K. A. Mohammed, R. Pandey and J. Madan, *Energy Fuels*, 2023, **37**, 7380–7400.
41 N. Shrivastav, S. Kashyap, J. Madan, A. K. Al-Mousoi, M. K. A. Mohammed, M. K. Hossain, R. Pandey and J. Ramanujam, *Energy Fuels*, 2023, **37**, 3083–3090.
42 H. Bencherif, F. Meddour, M. H. Elshorbagy, M. K. Hossain, A. Cuadrado, M. A. Abdi, T. Bendib, S. Kouda and J. Alda, *Micro Nanostruct.*, 2022, **171**, 207403.
43 Y. Raoui, H. Ez-Zahraouy, N. Tahiri, O. El Bounagui, S. Ahmad and S. Kazim, *Sol. Energy*, 2019, **193**, 948–955.
44 N. Touafek, R. Mahamdi and C. Dridi, *Dig. J. Nanomater. Biostructures*, 2021, **16**, 705–712.
45 L. Moulaoui, O. Bajjou, A. Najim, M. Archi and K. Rahmani, in *2022 2nd International Conference on Innovative Research in Applied Science, Engineering and Technology (IRASET)*, IEEE, 2022, pp. 1–7.
46 M. M. Khatun, A. Sunny and S. R. Al Ahmed, *Sol. Energy*, 2021, **224**, 956–965.
47 Y. H. Khattak, F. Baig, H. Toura, S. Beg and B. M. Soucase, *J. Electron. Mater.*, 2019, **48**, 5723–5733.
48 M. K. Hossain, G. F. I. Toki, J. Madan, R. Pandey, H. Bencherif, M. K. A. Mohammed, M. R. Islam, M. H. K. Rubel, M. F. Rahman, S. Bhattarai and D. P. Samajdar, *New J. Chem.*, 2023, **47**, 8602–8624.
49 S. Kashyap, J. Madan, M. K. A. Mohammed, M. K. Hossain, S. Ponnusamy and R. Pandey, *Mater. Lett.*, 2023, **339**, 134096.
50 M. K. Hossain, G. F. I. Toki, D. P. Samajdar, M. Mushtaq, M. H. K. Rubel, R. Pandey, J. Madan, M. K. A. Mohammed, M. R. Islam, M. F. Rahman and H. Bencherif, *ACS Omega*, 2023, **8**, 22466–22485.

© 2023 The Author(s). Published by the Royal Society of Chemistry

Open Access Article. Published on 04 August 2023. Downloaded on 2/24/2026 8:13:02 PM. This article is licensed under a Creative Commons Attribution-NonCommercial 3.0 Unported Licence.

51 M. F. Rahman, N. Mahmud, I. Alam, M. H. Ali, M. M. A. Moon, A. Kuddus, G. F. I. Toki, M. H. K. Rubel, M. A. Al Asad and M. K. Hossain, *AIP Adv.*, 2023, **13**, 045309.
52 A. Isha, A. Kowsar, A. Kuddus, M. K. Hossain, M. H. Ali, M. D. Haque and M. F. Rahman, *Heliyon*, 2023, **9**, e15716.
53 M. E. Islam, M. R. Islam, S. Ahmmed, M. K. Hossain and M. F. Rahman, *Phys. Scr.*, 2023, **98**, 065501.
54 M. K. A. Mohammed, A. K. Al-Mousoi, S. Singh, A. Kumar, M. K. Hossain, S. Q. Salih, P. Sasikumar, R. Pandey, A. A. Yadav and Z. M. Yaseen, *Opt. Mater.*, 2023, **138**, 113702.
55 M. F. Rahman, M. M. Alam Moon, M. K. Hossain, M. H. Ali, M. D. Haque, A. Kuddus, J. Hossain and A. B. Md. Ismail, *Heliyon*, 2022, **8**, e12034.
56 M. Burgelman, P. Nollet and S. Degrave, *Thin Solid Films*, 2000, **361–362**, 527–532.
57 M. Hasan Ali, A. T. M. Saiful Islam, M. D. Haque, M. Ferdous Rahman, M. Khalid Hossain, N. Sultana and A. Z. M. Touhidul Islam, *Mater. Today Commun.*, 2023, **34**, 105387.
58 M. F. Rahman, M. J. A. A. Habib, M. H. Ali, M. H. K. K. Rubel, M. R. Islam, A. B. Md. Ismail and M. K. Hossain, *AIP Adv.*, 2022, **12**, 105317.
59 M. H. Ali, M. A. Al Mamun, M. D. Haque, M. F. Rahman, M. K. Hossain, A. Z. Md and T. Islam, *ACS Omega*, 2023, **8**, 7017–7029.
60 E. H. Ihalane, L. Atourki, H. Kirou, A. Ihlal and K. Bouabid, *Mater. Today: Proc.*, 2016, **3**, 2570–2577.
61 R. T. Mouchou, T. C. Jen, O. T. Laseinde and K. O. Ukoba, *Mater. Today: Proc.*, 2021, **38**, 835–841.
62 F. Behrouznejad, S. Shahbazi, N. Taghavinia, H.-P. Wu and E. Wei-Guang Diau, *J. Mater. Chem. A*, 2016, **4**, 13488–13498.
63 M. K. Hossain, D. P. Samajdar, R. C. Das, A. A. Arnab, M. F. Rahman, M. H. K. Rubel, M. R. Islam, H. Bencherif, R. Pandey, J. Madan and M. K. A. Mohammed, *Energy Fuels*, 2023, **37**, 3957–3979.
64 L. Lin, L. Jiang, P. Li, B. Fan and Y. Qiu, *J. Phys. Chem. Solids*, 2019, **124**, 205–211.
65 A. Gheno, T. T. Thu Pham, C. Di Bin, J. Bouclé, B. Ratier and S. Vedraine, *Sol. Energy Mater. Sol. Cells*, 2017, **161**, 347–354.
66 O. Ahmad, A. Rashid, M. W. Ahmed, M. F. Nasir and I. Qasim, *Opt. Mater.*, 2021, **117**, 111105.
67 P. K. Patel, *Sci. Rep.*, 2021, **11**, 3082.
68 M. K. Hossain, G. F. I. Toki, I. Alam, R. Pandey, D. P. Samajdar, M. F. Rahman, M. R. Islam, M. H. K. Rubel, H. Bencherif, J. Madan and M. K. A. Mohammed, *New J. Chem.*, 2023, **47**, 4801–4817.
69 N. Lakhdar and A. Hima, *Opt. Mater.*, 2020, **99**, 109517.
70 A. Mohandes, M. Moradi and H. Nadgaran, *Opt. Quantum Electron.*, 2021, **53**, 1–22.
71 Y. Cao, X. Zhu, H. Chen, X. Zhang, J. Zhouc, Z. Hu and J. Pang, *Sol. Energy Mater. Sol. Cells*, 2019, **200**, 109945.
72 R. R. K. Raghvendra and S. K. Pandey, *Superlattices Microstruct.*, 2019, **135**, 106273.
73 S. Rühle, M. Shalom and A. Zaban, *ChemPhysChem*, 2010, **11**, 2290–2304.
74 J. Du, Z. Du, J. S. Hu, Z. Pan, Q. Shen, J. Sun, D. Long, H. Dong, L. Sun, X. Zhong and L. J. Wan, *J. Am. Chem. Soc.*, 2016, **138**, 4201–4209.
75 M. K. Hossain, S. Bhattarai, A. A. Arnab, M. K. A. Mohammed, R. Pandey, M. H. Ali, M. F. Rahman, M. R. Islam, D. P. Samajdar, J. Madan, H. Bencherif, D. K. Dwivedi and M. Amami, *RSC Adv.*, 2023, **13**, 21044–21062.
76 M. H. Kumar, S. Dharani, W. L. Leong, P. P. Boix, R. R. Prabhakar, T. Baikie, C. Shi, H. Ding, R. Ramesh, M. Asta, M. Graetzel, S. G. Mhaisalkar and N. Mathews, *Adv. Mater.*, 2014, **26**, 7122–7127.
77 M. S. Rahman, S. Miah, M. S. W. Marma and M. Ibrahim, *IEEE Reg. 10 Annu. Int. Conf. Proceedings/TENCON*, 2020, vol. 2020-Novem, pp. 140–145.
78 N. Wang, Y. Zhou, M.-G. Ju, H. F. Garces, T. Ding, S. Pang, X. C. Zeng, N. P. Padture and X. W. Sun, *Adv. Energy Mater.*, 2016, **6**, 1601130.
79 T. A. Chowdhury, M. A. Bin Zafar, M. Sajjad-Ul Islam, M. Shahinuzzaman, M. A. Islam and M. U. Khandaker, *RSC Adv.*, 2023, **13**, 1787–1810.
80 N. K. Noel, S. D. Stranks, A. Abate, C. Wehrenfennig, S. Guarnera, A. A. Haghighirad, A. Sadhanala, G. E. Eperon, S. K. Pathak, M. B. Johnston, A. Petrozza, L. M. Herz and H. J. Snaith, *Energy Environ. Sci.*, 2014, **7**, 3061–3068.

© 2023 The Author(s). Published by the Royal Society of Chemistry